CATCH OF THE NET

Solar storms are caused by the sudden release of magnetic energy stored in the Sun's atmosphere. In an event called a coronal mass ejection (CME), bursts of charged particles are released into space. CMEs that are big enough can collide directly with Earth's magnetosphere, the magnetic envelope that surrounds the planet, resulting in intense magnetic field variations that induce electric fields over large areas of Earth's surface. This geoelectric field creates geomagnetically induced currents (GICs) which flow in any available conductor, including high-voltage transmission lines, oil and gas pipelines, railways, and undersea communications cables. This causes interference for technologies such as electrical power grids, communications systems and satellites, including satellite navigation (sat-nav) signals. For example, on 13 March 1989, a solar storm, occurring during a solar maximum, took down Quebec's entire power grid, leaving 6 million people without power for 12 hours, and caused over 200 power grid problems in the US. The storm also caused some satellites to lose control for several hours, such as NASA's TDRS-1 communications satellite which recorded over 250 anomalies due to disruption of its sensitive electronics. The 1989 solar storm was much smaller compared to more powerful storms that occurred in 1859 and 1921. According a 2008 report of the US National Research Council, a storm of similar magnitude could cause $1-2 trillion in damage globally. With the next solar maximum expected to occur in late 2012 or 2013, there is increasing concern as to the vulnerabilities of existing technologies and infrastructures to solar storms. The following are relatively interesting and useful websites on solar storms and their effects:

1) **Solarstorms.org**
   http://www.solarstorms.org

2) **IEEE Spectrum: A Perfect Storm of Planetary Proportions**
   http://spectrum.ieee.org/energy/the-smarter-grid/a-perfect-storm-of-planetary-proportions
   Critical analyses of the vulnerabilities of various technologies and infrastructures to solar storms.

3) **National Oceanic and Atmospheric Administration (NOAA) Space Weather Scales**
   http://www.swpc.noaa.gov/NOAAscales
   Discusses the G-scale, which is the most commonly employed method of gauging solar storm intensity. The scale rates storms from 1, the least severe, to a maximum of 5.

4) **NOAA Space Weather Center**
   http://www.swpc.noaa.gov

5) **Spaceweather.com**
   http://www.spaceweather.com

6) **SolarHam.com**
   http://www.spaceweather.com
   Resource centres for space weather, including data, predictions and warnings.

7) **Ionospheric Prediction Service (IPS) Radio and Space Services**
   http://www.swpc.noaa.gov/NOAAscales
   The Australian space weather service, with particular emphasis on radio interference issues caused by solar storms.

8) **Solar and Heliospheric Observatory (SOHO)**
   http://sohowww.nascom.nasa.gov

9) **Advanced Composition Explorer (ACE)**
   http://www.srl.caltech.edu/ACE
   Provides space weather data collected by the SOHO and ACE satellites respectively, which orbit around the First Lagrangian Point (L1), where the combined gravity of the Earth and Sun keep the satellites' orbits locked to the Earth-Sun line.

DEFENCE S&T TECHNICAL BULLETIN

VOL. 5 | NUM. 1 | YEAR 2012 | ISSN 1985-6571

CONTENTS

STRIDE™

SCIENCE & TECHNOLOGY RESEARCH INSTITUTE FOR DEFENCE

ISSN 1985-6571

AIMS AND SCOPE

The Defence S&T Technical Bulletin is the official technical bulletin of the Science & Technology Research Institute for Defence (STRIDE). It contains articles on research findings in various fields of defence science & technology. The primary purpose of this bulletin is to act as a channel for the publication of defence-based research work undertaken by researchers both within and outside the country.

WRITING FOR THE DEFENCE S&T TECHNICAL BULLETIN

Contributions to the bulletin should be based on original research in areas related to defence science & technology. All contributions should be in English.

PUBLICATION

The editors' decision with regard to publication of any item is final. A paper is accepted on the understanding that it is an original piece of work which has not been accepted for publication elsewhere. Contributors will receive two complimentary copies of the issue in which their work appears.

PRESENTATION OF MANUSCRIPTS

The format of the manuscript is as follows:

a) Page size B5 (JIS)
b) MS Word format
c) Single space
d) Justified
e) In Times New Roman ,11-point font
f) Should not exceed 20 pages, including references
g) Texts in charts and tables should be in 10-point font.

Please e-mail the manuscript to:

1) Dr. Zalini bt Yunus (zalini.yunus@stride.gov.my)
2) Dr. Mahdi bin Che Isa (mahdi.cheisa@stride.gov.my)
3) Dinesh Sathyamoorthy (dinesh.sathyamoorthy@stride.gov.my)

The next edition of the bulletin is expected to be published in November 2012. The due date for submissions is 19 September 2012. **It is strongly iterated that authors are solely responsible for taking the necessary steps to ensure that the submitted manuscripts do not contain confidential or sensitive material.**

The template of the manuscript is as follows:

TITLE OF MANUSCRIPT

Name(s) of author(s)

Affiliation(s)

E-mail:

ABSTRACT

Contents of abstract.

Keywords: *Keyword 1; keyword 2; keyword 3; keyword 4; keyword 5.*

1. TOPIC 1

Paragraph 1.

Paragraph 2.

1.1 Sub Topic 1

Paragraph 1.

Paragraph 2.

2. TOPIC 2

Paragraph 1.

Paragraph 2.

Figure 1: Title of figure.

Table 1: Title of table.

Content	**Content**	**Content**
Content	Content	Content
Content	Content	Content
Content	Content	Content

Equation 1 (1)
Equation 2 (2)

REFERENCES

Long lists of notes of bibliographical references are generally not required. The method of citing references in the text is 'name date' style, e.g. 'Hanis (1993) claimed that...', or '…including the lack of interoperability (Bohara *et al.*, 2003)'. End references should be in alphabetical order. The following reference style is to be adhered to:

Books

Serra, J. (1982). *Image Analysis and Mathematical Morphology*. Academic Press, London.

Book Chapters

Goodchild, M.F. & Quattrochi, D.A. (1997). Scale, multiscaling, remote sensing and GIS. *In* Quattrochi, D.A. and Goodchild, M.F. (Eds.), *Scale in Remote Sensing and GIS*. Lewis Publishers, Boca Raton, Florida, pp. 1-11.

Journals / Serials

Jang, B.K. & Chin, R.T. (1990). Analysis of thinning algorithms using mathematical morphology. *IEEE T. Pattern Anal.*, **12**: 541-550.

Online Sources

GTOPO30 (1996). *GTOPO30: Global 30 Arc Second Elevation Data Set*. Available online at: http://edcwww.cr.usgs.gov/landdaac/gtopo30/gtopo30.html (Last access date: 1st June 2009)

Unpublished Materials (e.g. theses, reports and documents)

Wood, J. (1996). *The Geomorphological Characterization of Digital Elevation Models*. PhD Thesis, Department of Geography, University of Leicester, Leicester.

CHARACTERISATION OF CARBON DIOXIDE ABSORBENT MATERIAL FOR ENCLOSED SPACE APPLICATIONS

Mahdi Che Isa[1*], Nik Hassanuddin Nik Yusoff[1], Mohd Subhi Din Yati[1], Mohd Moesli Muhammad[1], Nor Afizah Salleh[2], Mohd Fauzy Mohd Nor[2], Azmi Minal[2] Hasril Nain[3] & Irwan Mohd Nor[1]

[1]Materials Research Group, Maritime Technology Division (BTM)
[2]Weapons Technology Division (BTP)
Science & Technology Research Institute for Defence (STRIDE), Ministry of Defence, Malaysia
[3]Ship Silencing Centre (SSC), Royal Malaysian Navy (RMN), Malaysia

[*]Email: mahdi.cheisa@stride.gov.my

ABSTRACT

Soda lime is one of the most popular absorbent materials used for eliminating carbon dioxide (CO_2) from contaminated air. Variation in soda lime chemical composition and physical properties influence its final performance for specific applications. Parameters such as chemical composition, moisture absorption, loss on dryness, granules shape, chemical absorbency and particle (dust) sizes play a very important role in determining the quality and life span of soda lime materials. This paper discusses the results of characterisation and evaluation conducted by STRIDE on a commercial soda lime material. This study shows that the sample is a mixture of calcium hydroxide, sodium hydroxide and moisture. The sample has been produced to provide soda lime granules with optimised surface area, hardness, and toughness for resistance to abrasion, uniformity in mesh size, and consistency in quality.

Keywords: *Carbon dioxide (CO_2); soda lime; submarine atmosphere; air quality; hardness; chemical composition.*

1. INTRODUCTION

The revitalisation of air present in the atmosphere of all natures is of great importance. This applies for any type of atmosphere, be that of a space capsule, a submarine or any enclosed compartment (Douglas *et al.*, 1989). The atmosphere factor within the enclose system is vital for life, and hence air purification has been introduced to remove contaminants or any types of toxic gases, in order to maintain a healthy air composition. For example, excess amount of carbon dioxide (CO_2) should be removed, and this can be done either by chemical separation technology or physical adsorption process (Olajire, 2010; Hsu & Chung, 2011).

The air purification system employed should be capable of maintaining appropriate CO_2 and oxygen levels so that it will not impair mental and physical performances. At 1% CO_2 content, the enclosed environment must be ventilated, and / or preparation made to remove the gas (Jonathan *et al.*, 2009; Cable, 2008). CO_2 absorbent materials are well known and widely used in a number of applications. They may include, for example, in a variety of industries, such as anaesthesia, respiratory care, hyperbaric chambers, military and tourist submarines, underwater diving gear, fire safety apparatus, and mine rescue equipment. Monoethanolamine (MEA), zeolite molecular sieves, baralime (a mixture of 80% calcium hydroxide and 20% barium hydroxide), soda lime and lithium hydroxide (LiOH) are typical absorbents used to scrub CO_2 from the air (Leci *et al.*, 1992; Plaza *et al.*, 2009; Dugas *et al.*, 2009; Llano-Restrepo, 2010). Of these materials, the most commonly used absorbents in submarines are MEA and soda lime (Carey *et al.*, 1983; Mazurek, 2005).

Soda lime, the most popular absorbent, was originally developed by Prof. Robert E. Wilson of Massachusetts Institute of Technology (MIT) in the year 1917 to meet the urgent need for an effective absorbent in military gas masks to absorb soldiers' exhaled CO_2 (Moore & Campbell, 1983). When exposed to atmospheric CO_2 under moist conditions, soda lime reacts and converts into calcium carbonate as a result of carbonation. Soda lime is an absorbent material which contains a certain composition of calcium hydroxide (slaked lime), metal oxide and water contents. As it reacts with CO_2, it forms a stable solid which is retained within the absorbent canister (Lillo *et al.*, 1996; Renato *et al.*, 2006). For safety reasons, an appropriate reserve quantity of soda lime is essential if CO_2 content reaches 1% of any enclose space volume and the removal process of CO_2 should then start to progress.

Particle size and shape, porosity, and bulk density are particularly important in terms of the performance of an absorbent material in its intended application. Most soda lime grades are now produced with shapes that offer high surface to volume ratio. These carefully engineered shapes ensure maximum CO_2 penetration into the particles, by minimising the distance to the centre of the particles, thereby increasing the CO_2 capacity of the product. Variations in conditions, such as humidity, can significantly affect the predicted life expectancy and performance of the absorbent (Shunji *et al.*, 2003; Klos, 2008). Another key factor in determining absorbent performance is particle size distribution. Particle size has an effect on the speed of reaction, which in turn affects the volume of the reaction zone and the capacity of the absorbent. In general terms, the smaller the particle size, the smaller the reaction zone volume that results to higher reactions. However, the smaller the particle size, the greater the pressure-drop across the absorbent, which may affect absorption efficiency and other characteristics (Mazurek, 2005).

The aims of this study are to determine the chemical composition of a selected commercial soda lime material and to characterise its physical properties, with respect to granules size distribution, hardness, moisture contents and chemical

reactivity. The data obtained from this study will be compared with standards of the same product for the purpose of air regeneration process in enclosed spaces, particularly for submarine applications.

2. MATERIALS & METHODS

A commercial 4.5 kg soda lime sample obtained from Scientific Engineering & Technology Services (SETS), Rawalpindi, Pakistan, was selected for this study. The physical appearance of its granules was observed using a normal digital camera, while the sizes of the granules were determined using a stereomicroscope with image analyser (Carl Zeiss Axio Vision). Particle or dust size measurement was carried out by screening 100 g of the sample for 5 min using a mechanical shaker, with a Num. 45 (355 μm) standard-mesh sieve. The hardness of the sample was determined by shaking 200 g on a sieve with size 425 micron for 5 min using a mechanical sieve shaker. Of the retained material, 50 g was placed in a hardness pan having a concave brass bottom, diameter of 20 cm, thickness of 7.9 mm at the circumference and 3.2 mm at the centre, and inside spherical radius of curvature of 109 cm. A total of 15 steel balls with diameter of 7.9 mm were added and the mechanical sieve shaker was operated for 30 min. The steel balls were removed, and the contents of the pan were transferred to the sieve and shaked on the mechanical sieve shaker for 5 min. The material retained on the sieve was weighed.

The loss on drying test was carried out by placing 10 g of the sample in an oven for 2 h at 105 °C. For the moisture absorption test, 10 g is placed in a 50 ml weighing bottle, having diameter of 50 mm and height of 30 mm, and its cover removed. The bottle was stored for 24 h in a closed container in which the atmosphere was maintained at 85% relative humidity (RH) by being in equilibrium with sulfuric acid having a specific gravity of 1.16, which is the requirement set by USP-NF (2010). The final weight of the sample was recorded.

The phases presence in the soda lime material were determined using an X-ray diffractometer (XRD) (Bruker D8-Advanced) housed at the School of Applied Physics, National University of Malaysia (UKM). The diffractogram was generated using a Cu Kα ($\lambda = 1.543$ Å) radiation source at scanning rate of 0.002 °/s with 2θ from 20º to 60º.

The elemental composition of the material was analysed using a wavelength dispersive X-ray fluorescence (XRF) spectrometer (Bruker SP 4 Pioneer, WDXRF) equipped with an Rh X-ray tube and 4 kW generator. The X-ray generator was operated at voltage of 20 - 50 kV and current of 5-20 mA.To prepare the XRF-pellet, a small metallic sample holder made of aluminium with diameter of 3 cm was used. The pellets were pressed for 30 s with pressure of 10 tons/cm^2 using the Specac hydraulic press machine. From this process, the total mass of each pellet gained was 10.8 g.

Quantitative calculations were made using the accompanied software. The results of the analysis were expressed in weight percentage (*wt.%*).

To determine the chemical absorbency of the sample, an amount of 33.3 g is placed inside a U-tube with 10 g of calcium chloride ($CaCl_2$) to trap the moisture produced by the neutralisation reaction and to simulate dry environments. 99.5% purified CO_2 gas was injected/inserted/ through the U-tube at the rate of 1,000 ml per minutes for five minutes to allow it to cool down. The initial and final weights of the U-tube were recorded to determine the permissible quantity of CO_2 which had been absorbed by the soda lime.

3. RESULTS & DISCUSSION

The physical appearance of the soda lime granules is shown in Figure 1. The granules have non-uniform, irregular shapes with diameters in the range of 3-7 mm as shown in Figure 2. Table 1 shows various distribution size of granules. It was observed that 76.8% of granules were in the range of 2.36 - 4.75 mm in diameter. The current size distribution of the granules can be considered as a compromise between resistance to air flow and absorptive capacity of the soda lime material.

Figure 1: Photograph of the near white or greyish white soda lime granules.

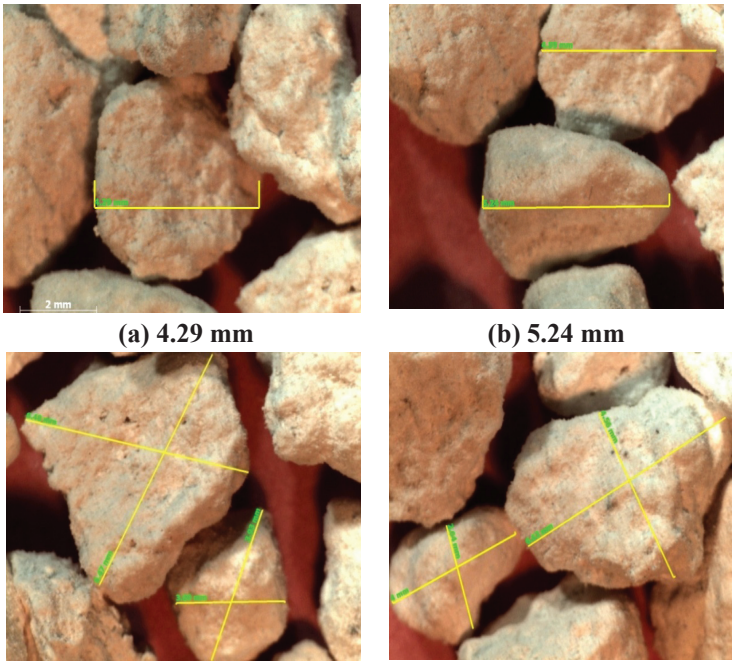

(a) 4.29 mm (b) 5.24 mm

(c) 3.69 mm and 6.48 mm (d) 3.21 mm and 5.99 mm

Figure 2: Variations of the soda lime granules' diameters.

Table 1: The soda lime granules' size distribution.

Granule size (diameter)	%
More than 5.6 mm	0.7
4.75-5.60 mm	21
2.36-4.75 mm	76.8
0.60-2.36 mm	1
Less than 0.6 mm	0.5

The particle size determination results in Table 2 showed that not more than 2.0% of the sample (average of only 0.64%) passed through a Num. 45 standard-mesh sieve (USF-NF, 2010). The presence of dust in the sample is also in good agreement with the specification set by NATO (2006), which requires that not more than 1% of the particles should be below 600 µm. The low dust content indicates that there was only a small amount of sharp edges of the granules which rubbed against one another during processing, transporting and storing activities. The hardness test conducted gave a result of 81.16%, which is in compliance with USP-NF (2010), indicating that the sample is not too soft or friable, and not easily broken down to form underparticles or dust.

Table 2: Results of the particle size test using a Num. 45 (355 µm) standard mesh sieve.

No. of tests	% pass through
1	0.4251
2	0.7807
3	0.7265
Total	**1.9323**
Average	***0.6441***

The sample recorded 13.45 % loss of weight on drying. This is within the tolerance of soda lime specifications that requires 12 to 19 % of weight at 105 °C for 2 h.. In addition, for storage purposes and shelf life of soda lime, its weight shall not increase more than 7.5% after being stored in a closed container for 24 h. The sample only undergoes 0.86% weight increase, which satisfies the requirement of USP-NF (2010).

The elemental composition of soda lime is shown in Table 3. The main metal oxides determined by the WDXRF machine were calcium hydroxide ($Ca(OH)_2$) (87.0%), sodium hydroxide (NaOH) (10.2%) and silicon dioxide (SiO_2) (0.9%). In this sample, we believe a small amount of Si was added to produce calcium and sodium silicate. This addition produces a harder and more stable soda lime granule, and thereby, reduces dust formation as recorded in Table 2. Elements other than Ca, Na and Si were also detected, which are impurities from raw materials, strongly believed to be from the grades of purity of calcium oxide (CaO) used in the soda lime manufacturing process.

Table 3: The elemental composition of the sample

No.	Elements	wt.%
1.	Calcium (Ca)	87.0
2.	Sodium (Na)	10.2
3.	Silicon (Si)	0.9
4.	Magnesium (Mg)	0.5
5.	Strontium (Sr)	0.4
6.	Aliminium (Al)	0.1
7.	Iron (Fe)	0.2
8.	Sulphur (S)	0.2
9.	Others (total)	0.5

Figure 3 shows the XRD spectrum for the sample with the presence of major peaks for the $Ca(OH)_2$ and NaOH phases. Based on the XRD results, it can be concluded that the sample consists of a mixture of $Ca(OH)_2$ and NaOH. However, the XRD spectrum also shows a very broad diffraction pattern where the presence of low intensity peaks identified as vaterite phase (µe-$CaCO_3$; JCPDS* 33-0268) can be clearly seen. Vaterite is associated to the presence of monohydrocalcite ($CaCO_3.H_2O$;

* Joint Committee on Powder Diffraction Standards

JCPDS 29-0306) and a small amount of calcite ($CaCO_3$; JCPDS 01-086-2342 R-3c) (Lopez-Arce *et al.*, 2010). The presence of the vaterite phase in the sample can be attributed to the reaction between CO_2 in the air and $Ca(OH)_2$ in the sample.

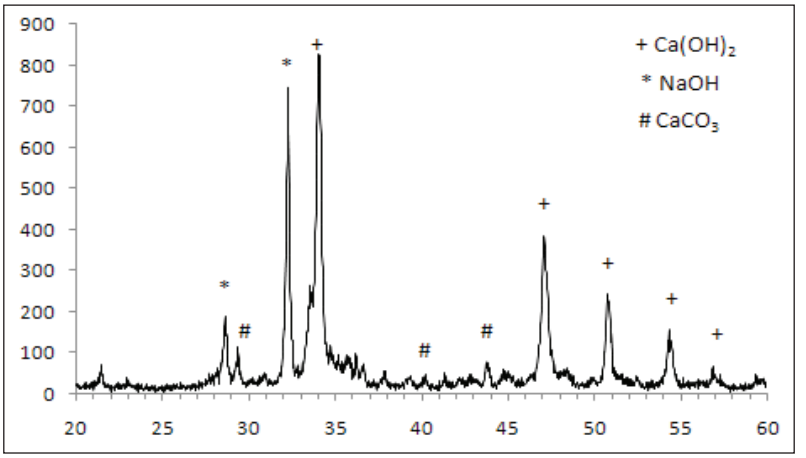

Figure 3: XRD spectrum for the sample.

The CO_2 absorption reaction occurred according to Equation 1 in which CO_2 reacts with $Ca(OH)_2$ to produce vaterite or calcium carbonate, and water. This reaction took place during the sample preparation and / or during exposure to atmosphere during the XRD testing procedures (Randell & Clarke, 2003). Based on this, it can be concluded that XRD analysis is capable of revealing the fast transformation or reaction of the sample with CO_2 in the air to form vaterite (metastable $CaCO_3$), monohydrocalcite ($CaCO_3.H_2O$) and calcite ($CaCO_3$) in high humidity conditions (RH 80%).

$$CO_2\,(g) + Ca(OH)_2\,(s) \rightarrow CaCO_3\,(s) + H_2O\,(g, l) + Heat \qquad (1)$$

The presence of strong alkali hydroxides (NaOH) allows the sample to absorb CO_2 more quickly and with greater capacity than mixtures containing only lime and water. The absorption performance of soda lime is very important, thus the scrubbing capacity and life expectancy shall be predicted based on a given set of conditions. Variations in conditions of flow rate, CO_2 concentration, temperature, pressure, humidity etc. can significantly affect the predicted life expectancy (Randel *et al.*, 2003).

One of the important properties of soda lime granules is morphology (physical form and shape) because the surface to volume ratio is very important in determining how fast the material can react and chemical absorption capacity. To produce good gas-solid interaction behaviour, more surface path for the gas through the granules with less straight channels should be designed. For some granules with very uniform shape, this can readily lead to large straight channels forming, which tend to leave unreacted material at its centre as it is a long way from the surface to the centre (Audrius *et al.*, 1996).

Therefore, in order to minimise the unreacted zone, the irregular shaped granules in the sample can provide an absorbent material which can provide higher surface area, facilitate more reaction sites, and increase reaction rates. Based on the results of the chemical absorbency test (Table 4), the sample achieved the minimum CO_2 absorption specified by USP-NF (2010), which states that the weight increment of the sample after test shall be not less than 19%. The optimum physical properties together with the presence of alkali metal hydroxides in the sample are believed to contribute towards the improvement of absorbency of CO_2 (Baum & Woehlck, 2003). This finding is in good agreement with studies conducted by previous researchers which have claimed that CO_2 absorbents that contain small amounts of NaOH (3.2%) have greater CO_2 absorption capacity than absorbents that do not contain NaOH (Stabernack *et al.*, 2000).

Table 4: Results of the chemical absorbency test.

Num. of tests	% of weight increment
1	21.36
2	22.28
3	20.68
Average	**21.44**

4. CONCLUSION

The results obtained from our characterisation works show that the quality of the selected commercial soda lime product used as a CO_2 absorbent material complies with the requirements set by many industries, particularly for use in enclosed spaces and military applications. The sample is a mixture of $Ca(OH)_2$, NaOH and water, which has been produced in irregular shaped solid granules in order to maximise CO_2 absorption in the air. This study also shows that proper storing will prolong the sample's shelf life by minimising the amount of moisture absorbed, loss of weight during drying, and formation small sized particle (soda lime dust).

ACKNOWLEDGEMENT

The authors would like to thank the Government of Malaysia for financing this R&D project under the 10th Malaysia Plan. We also greatly appreciate Datuk Dr. Abdul Ghaffar bin Ramli, Director-General of STRIDE, for his support, ideas, and a series of meaningful and fruitful discussions. We wish to thank the Weapons Technology Division, STRIDE, for conducting the granules' size test, and Prof. Mohd Ambar Yarmo, from the Faculty of Science & Technology, UKM, for assisting and conducting the XRD test. We are pleased to acknowledge SETS, Pakistan, for

providing the soda lime samples, and Dr. Assanah Mohd Mydin from Caidmark Sdn. Bhd. for participating in this work. The cooperation and technical assistance given by STRIDE's officers and staff in improving the quality of this manuscript is also highly appreciated.

REFERENCES

Audrius M., Jolanta L. & Arunas Š. (1996). Regulation of cellulose-based absorbent granule morphology. *J Chrom. A*, **746**: 147-160.

Baum, J. A. & Woehlck, H. J. (2003). Interaction of inhalational anaesthetics with CO_2 absorbents. *Best Prac. Res. & Cl. An.*, **17**: 63-76.

Cable, J. (2008). *NIOSH Report Details The Dangers of Carbon Dioxide in Confined Spaces*. Available online at: http://www.occupationalhazards.com /News/ Article/37358 (Last access date: 24 December 2009).

Carey, R., Gomezplata, A. & Sarich, A. (1983). An overview into submarine CO_2 scrubber development. *Ocean Eng.*, **10**: 227-233.

Douglas, R. K., Donald, V. T., Jeffry, S. B., O'Neill, H. J. & Gordon, S. M. (1989). Submarine atmospheres. *Toxicol. Lett.,* **49**: 243-251.

Dugas, R., Alix, P., Lemaire, E., Broutin, P. & Rochelle, G. (2009). Absorber model for CO_2 capture by monoethanolamine - application to CASTOR pilot results. *Energy Procedia* **1**: 103-107.

Hsu H. C. & Chung S. T. (2011). Removal of CO_2 from indoor air by alkanolamine in a rotating packed bed. *Sep.Purif. Technol.*, **82**:156-166.

Jonathan L. S., David G. K. & Randal J. K. (2009). Occupational hazards of carbon dioxide exposure. *J. Chem. Health Safety*, **16**:18-22.

Klos, R. (2008). Removal of oxidable contaminations contained in submarine atmosphere. *Polish Maritime Res.*, **3**: 67-69.

Leci, C.L. & Goldthorpe, S.H. (1992). Assessment of CO_2 removal from power station flue gas. *Energy Converse. Manage.*, **33**: 477-485.

Lillo, R.S., Ruby, A., Gummin, D.D., Porter, W.R. & Caldwell, J.M. (1996). Chemical safety of U.S. Navy fleet soda lime. *Undersea Hyperbaric Med.*, **23**: 43-53.

Llano-Restrepo, M. (2010). Accurate correlation, structural interpretation, and thermochemistry of equilibrium adsorption isotherms of carbon dioxide in zeolite NaX by means of the GSTA. *Fluid Phase Equilibr.,* **293**: 225-236.

López-Arce, P., Gomez-Villalba, L.S., Pinho, L., Fernández-Valle, M.E., Álvarez de Buergo, M. & Fort, R. (2010). Influence of porosity and relative humidity on consolidation of dolostone with calcium hydroxide nanoparticles: Effectiveness assessment with non-destructive techniques. *Mat. Charac.,* **61**: 168-184.

Mazurek, W. (2005). Submarine atmosphere. In Hocking, M.B. & Hocking, D. (Eds.), *The Handbook of Environmental Chemistry: Vol. 4, Part H (Air Quality in Airplane Cabins and Similar Enclosed Spaces)*. Springer-Verlag Berlin Heiderberg, Germany, pp. 351-382.

Moore, L.W & Campbell, D.L. (1983). Robert Erastus Wilson. *In* National Academy of Sciences (Ed.), *Biographical Memoir*. National Academy of Sciences, Washington D.C., pp. 409-433

North Atlantic Treaty Organization (NATO) (2006). *NATO STANAG 1411: Standard to Quantify the Characteristics of Carbon Dioxide (CO_2) Absorbent Material for Diving, Submarine and Marine Applications*. North Atlantic Treaty Organization (NATO), Brussels.

Olajire, A.A. (2010). CO_2 capture and separation technologies for end-of-pipe applications – A review. *Energy,* **35**: 2610-2628.

Plaza, J.M., Wagener, D.V. & Rochelle, G.T. (2009). Modeling CO_2 capture with aqueous monoethanolamine. *Energy Procedia,* **1**: 1171-1178

Randell D.J. & Clarke, M. (2003). *Fourth International Conference on Submarine Air Monitoring And Air Purification* (*SAMAP),* Emden, Germany

Renato, B., Giuseppe, S. & Marco, M. (2006). Process design and energy requirements for the capture of carbon dioxide from air. *Chem. Eng. & Process.*, **45;** 1047 – 1058.

Rendell, D.J., Clarke, M. & Evans, M.. (2003). The effect of environmental conditions on the absorption of carbon dioxide using soda lime. *39th International Conference on Environmental Systems*, 12-16 July 2009, Hyatt Regency, Savannah, Georgia.

Shunji, K, Hiromichi, B. Takasumi, K. & Shigehito, S. (2003). Effect of humidity in the circuit on the CO_2 absorption capacity of Amsorb and Sodasorb II. *J Anesth,* **17**: 145-146

Stabernack, C.R., Brown, R., Laster, M.J., Dudziak, R. & Eger, E. (2000) Absorbents differ enormously in their capacity to produce compound A and carbon monoxide. *Anesth Analg*., **90**:1428–1435

USP–NF. (2010). *United States Pharmacopeia (USP) and the National Formulary (NF)*. Available online at: http://www.usp.org/USPNF (Last access date: 26 August 2010).

PRELIMINARY STUDY ON INDOOR AIR QUALITY (IAQ) ON A ROYAL MALAYSIAN NAVY (RMN) SHIP

Ridwan Yahaya*, Haryatti Mohd Arif & Siti Noriza Mohd Kamel

Protection and Biophysical Technology Division (BTPB), Science and Technology Research Institute for Defence (STRIDE), Ministry of Defence, Malaysia

*Email: ridwan.yahaya@stride.gov.my

ABSTRACT

In this study, the indoor air quality (IAQ) on a Royal Malaysian Navy (RMN) ship was investigated to determine indoor air pollutant concentrations and indoor climates on board while the ship's engine was not running. Eight parameters (carbon monoxide (CO), carbon dioxide (CO_2), total volatile organic compounds (TVOCs), formaldehyde (HCHO) and particulate matter (PM_{10}), temperature, relative humidity (RH) and air movement) were measured at twelve sampling sites using the grab sampling method. The recorded measurements were compared with the acceptable levels of the corresponding parameters set by the Department of Occupational Safety & Health's (DOSH) Industry Code of Practice on Indoor Air Quality 2010, and the American Bureau of Shipping's (ABS) Guide for Crew Habitability on Ships. Based on the assessment conducted, it was observed that there are sites on the ship with IAQ issues relating to high levels of CO_2 and HCHO, low temperature, high RH, and low ventilation rate (air movement). The other IAQ parameters investigated were in compliance with the acceptable levels.

Keywords: *Indoor air quality (IAQ); indoor air pollutants; indoor climate; sampling sites; grab sampling method;*

1. INTRODUCTION

Indoor air quality (IAQ) monitoring is important to maintain healthy indoor working environments. Poor indoor air quality can cause a variety of short and long-term health problems, including allergic reactions, respiratory problems, eye irritation, sinusitis, bronchitis and pneumonia (EPA, 1998; DOSH, 2010). To this end, many studies have been conducted on the IAQ on various modes of transportation, including cars, buses and trains (Chan *et al.*, 2003; Lau & Chan, 2003; Chien, 2007; Kadiyala & Kumar, 2011).

IAQ on ships is important as the periods that crew members spend on board are relatively longer as compared to other transportation modes. Furthermore, with

limited and confined spaces, crew members can be exposed to hazardous pollutants on board (Sun & Yun, 2010; Elsafty, 2010). In previous studies regarding IAQ on ships, Sun & Yan (2010) and Mahdi & Zalini (2010) reported that the levels of carbon monoxide (CO), carbon dioxide (CO_2) and particulate matter (PM_{10}) in engine rooms were much higher than the requirements set by the respective standards. This could have been due to the combined effect of leakage in exhaust emission systems and insufficient ventilation. Webster (1997) and Webster & Reynolds (2005) conducted assessments of IAQ on various types of ships, including cruise ships, passenger ferries and cargo vessels, and found high levels of total volatile organic compounds (TVOCs) and formaldehyde (HCHO). In addition, studies conducted by KRISO (2002), Jang *et al.* (2007) and Elsafty (2010) indicated high levels of dissatisfaction with indoor air and thermal environment.

In this study, the IAQ on a Royal Malaysian Navy (RMN) ship was investigated to determine indoor air pollutant concentrations and indoor climates on board while the ship's engine was not running. The study was conducted from selected sampling sites using the guidelines prescribed by the Department of Occupational Safety & Health's (DOSH) Industry Code of Practice on Indoor Air Quality 2010 (DOSH, 2010), and the American Bureau of Shipping's (ABS) Guide for Crew Habitability on Ships (ABS, 2001).

2. METHODOLOGY

2.1 Sampling Sites

This study was conducted on a corvette class ship which serves in the RMN's 24th Corvette Squadron. The ship is powered by diesel engines and the main spaces of the ship are distributed over two decks. The cabins in the ship are furnished with beds, writing desks and fabric curtains, and are centrally air conditioned. Non-flammable paint is used throughout the ship, while the flooring material of most of the cabins and rooms is painted steel plates.

A total of twelve sampling sites (Rooms 1-9, and the dining hall, kitchen and bridge) were selected throughout the ship. The selection of sampling sites was made based on accessibility and number of occupants. Concentrations of CO, CO_2, TVOC, HCHO and PM_{10} were measured at each sampling site. In addition to pollutant concentrations, indoor temperature, relative humidity (RH) and air movement were also measured simultaneously. All the parameters were measured via the grab sampling method using samplers that were placed between 75 to 120 cm from the floor at the centre of the rooms as per the guidelines set by DOSH (2010). The air conditioning systems were in operation when the sampling was conducted.

2.2 Measurement

Data collection was conducted using direct-reading instruments, including a Q-TRAK™ Plus IAQ monitor (TSI Inc.), a DUST-TRAK™ aerosol particle monitor (TSI Inc.), a VOC monitor, model PGM-7600 (RAE Systems), a Velocicalc™ Plus multi-parameter ventilation meter, model 8386 (TSI, Inc.) and a Formaldemeter™ htV HCHO meter (PPM Technology Ltd.). The IAQ monitor uses a non-dispersive infrared sensor for measuring CO_2 concentration, an electrochemical sensor for CO concentration, a thermistor for temperature, and a thin-film capacitive element for RH. These parameters were recorded using a survey mode at 1 s intervals. This mode was used to display the real-time readings of all the parameters simultaneously. The span set for concentrations of CO_2 and CO were 1,000 and 35 ppm respectively.

The aerosol particulate monitor detects particles in the air via optical scattering. It was used to measure the concentrations of particulate matter with aerodynamic diameter less than 10 μm (PM_{10}) in ambient air. The measurement was conducted at 1 min intervals at flow-rate of 1.7 ℓ/min.

The VOC monitor employs a photo-ionisation detector (PID) with a gas discharge lamp to measure TVOC, while the ventilation monitor uses constant-temperature anemometry to measure air movement. The HCHO meter uses electrochemical sensing technology to measure airborne HCHO concentrations. It collects single air samples upon initiation by the user, employs a sampling frequency of 1-3 min, and analyses the samples within 60 s.

2.3 Guidelines for Evaluating IAQ

For the purpose of this study, the guidelines set by DOSH's Industry Code of Practice on Indoor Quality 2010 (DOSH, 2010) were used. This code of practice applies to all industries in Malaysia, including the automotive industry. One of the primary aims of the code is to establish a set of maximum exposure limits for common indoor air contaminants, such as CO, CO_2 and respirable particulates. In addition, the guidelines set by ABS' Guide for Crew Habitability on Ships (ABS, 2001) were referred to for indoor climate requirements. The acceptable values indicated by these guidelines for the IAQ parameters investigated in this study are shown in Table 1.

Table 1: Guidelines for acceptable values for the IAQ parameters investigated in this study.

Parameter	DOSH (2010)	ABS (2001)
CO (ppm)	10	-
CO_2 (ppm)	1,000	-
TVOC (ppm)	3	-
PM_{10} (mg/m^3)	0.15	-
HCHO (ppm)	0.10	-
Temperature (°C)	23-26	*22 ± 1 / **18-26.50
RH (%)	40-70	30-70
Air movement (m/s)	0.15-0.50	0.50

*Non-adjustable air temperature
**Adjustable range of air temperature

3. RESULTS AND DISCUSSION

In this section, the IAQ of the selected sampling sites is assessed via comparison of the results of the measurements with the acceptable levels of the corresponding parameters set by DOSH (2010) and ABS (2001).

3.1 Carbon Monoxide (CO)

It was observed that for all of the sampling sites, CO was not detected. This is in contrast with the findings of Mahdi & Zalini (2010) and Sun & Yan (2010), whereby high levels of CO were found in engine rooms, perceivably due to carbon in fuels not being burned completely. It is probable that non-detection of CO in this study was because it did not involve the ship's engine room.

3.2 Carbon Dioxide (CO_2)

Based on the results shown in Figure 1, the CO_2 measurements for all the sampling sites exceeded the maximum limit of 1,000 ppm, with the exception of Rooms 6-8. The high levels of CO_2 could be due to overcrowding, in which the occupants were more than the number that the rooms were designed to hold. The highest CO_2 level was detected at Room 5, due to the high number of occupants (12) during sampling period. The high levels of CO_2 were also an indicator of poor performance of the ventilation system.

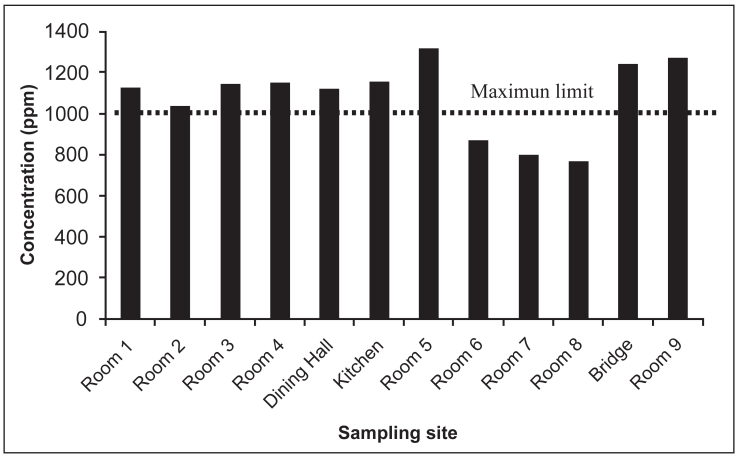

Figure 1: CO_2 levels of the sampling sites.

3.3 Total Volatile Organic Compounds (TVOCs)

It was found that none of the TVOC measurements (Figure 2) exceeded the maximum limit of 3 ppm set by DOSH (2010). The highest concentration detected during the sampling period was 1.21 ppm at the bridge. This indicates that there were no issues of chemical dispersion in the form of organic vapours.

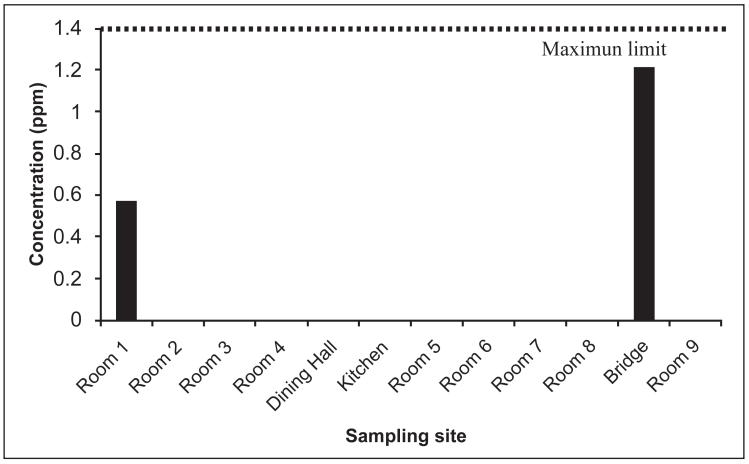

Figure 2: TVOC levels of the sampling sites.

3.4 Formaldehyde (HCHO)

Based on the results shown in Figure 3, it was found that two sampling sites (Rooms 2 and 3) had HCHO levels exceeding the maximum limit of 0.1 ppm. This indicates that there were issues of chemical dispersion and poor air dilution by the air conditioning

mechanical ventilation (ACMV) system. There could also be low ventilation and infiltration rates within the sites. Room 2 recorded the highest level of HCHO due to the usage of air fresheners or other type of fragrances, or due to the painting work that had been conducted prior to the measurement. It is important that when chemical based paint or thinner is used during the maintenance and refurbishment period, only the minimum number of crew members is allowed to be inside the ship due to high concentrations of HCHO.

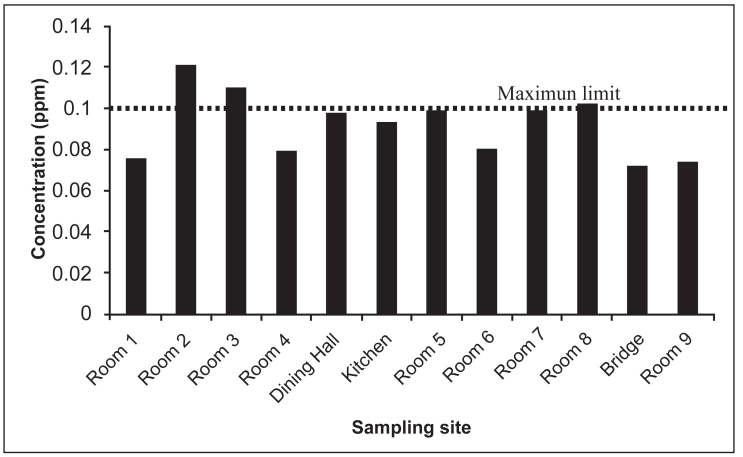

Figure 3: HCHO levels of the sampling sites.

3.5 Particulate Matter (PM_{10})

The PM_{10} measurements of all the sampling sites (Figure 4) were in compliance with the maximum limit of 0.15mg/m^3. Room 5 recorded the highest reading (0.149 mg/m^3) due to the high number of occupants. It is proposed that air cleaners be used in this room to reduce the high concentration of PM_{10}.

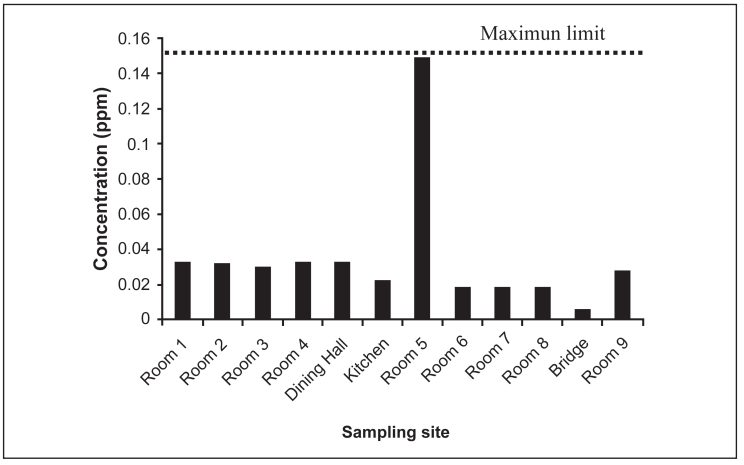

Figure 4: PM_{10} levels of the sampling sites.

3.6 Indoor Climate

3.6.1 Temperature

Based on the results shown in Figure 5, six sampling sites (Rooms 1-4 and 9, and the dining hall and kitchen) did not comply with the acceptable temperature range of 23-26 ^{o}C set by DOSH (2010), as they had temperature readings below the lower limit of 23 ^{o}C. These low temperature levels may be due to the air conditioning system operation, thermostat setting and type of ventilation method applied at the sites. However, all the measurements were in compliance with the acceptable temperature range of 18-26.5 °C set by ABS (2001).

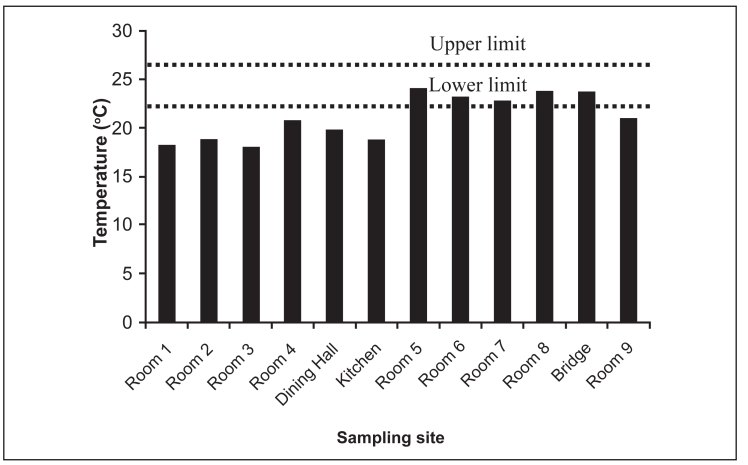

Figure 5: Temperature levels of the sampling sites.

3.6.2 Relative Humidity (RH)

Five sampling sites (Rooms 1, 3 and 4, and the dining hall and kitchen) did not comply with the acceptable RH ranges of 40-70 % and 30-70 % set by DOSH (2010) and ABS (2001) respectively, as they had RH levels above the upper limit of 70 % (Figure 6). High humidity may result in condensation within closed areas and may increase the potential of microbial growth (Brightman & Moss, 2000; Wolkoff & Kjægaard, 2007; Mahdi & Zalini, 2010).

Figure 7 shows the distribution of the measured temperature and RH levels on the ship. The dotted lines show the requirements based on DOSH (2010) and ABS (2001). It is observed that only seven of the sampling sites met the requirements of ABS (2001), while only five met the requirements of DOSH (2010).

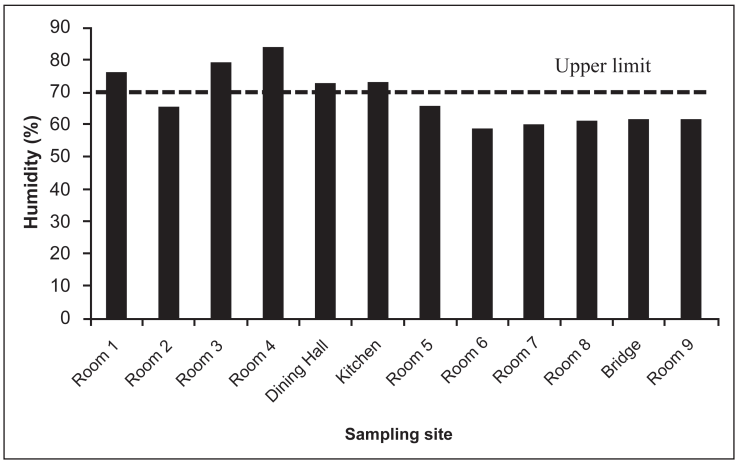

Figure 6: RH levels of the sampling sites.

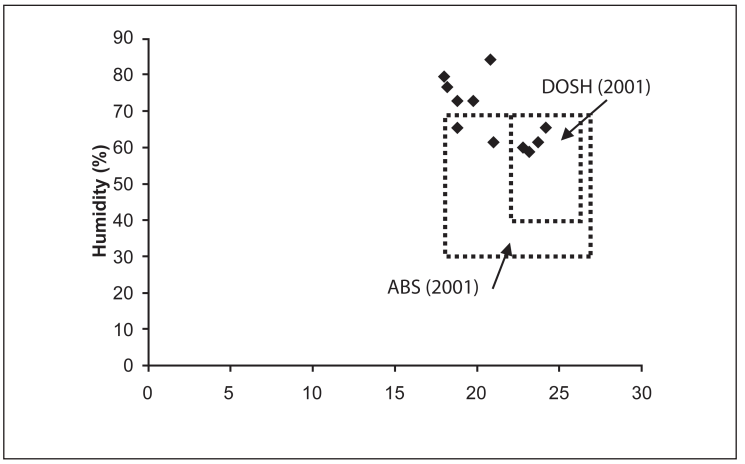

Figure 7: Distribution of the measured temperature and RH levels on the ship.

3.6.3 Air Movement

Air movement is an important factor in thermal comfort because stagnant air often contributes to a feeling of stuffiness and causes odour build-up, while even the smallest air movement in cold environments is often considered to be draughty (EPA, 1998; Brightman & Moss, 2000; Sundell, 2004; SEA, 2012). DOSH (2010) sets the acceptable level of air movement at 0.15-0.50 m/s, while ABS (2001) sets the upper limit at 0.50 m/s. This condition is described as a pleasant breeze. Based on the results shown in Figure 8, the air movement levels of all of the sampling sites, except Room 8 and bridge, did not comply with the acceptable range, as they were below the lower limit of 0.15 m/s.

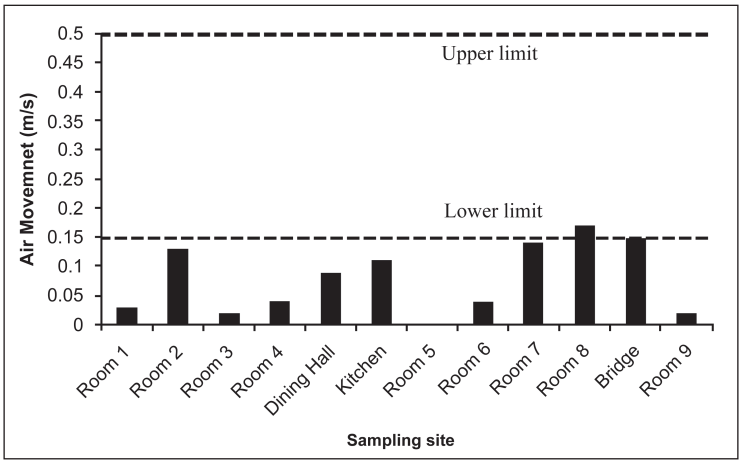

Figure 8: Air movement levels of the sampling sites.

4. CONCLUSION

Based on acceptable levels of IAQ parameters set by DOSH (2010) and ABS (2001), an assessment of IAQ on the RMN ship was conducted. The findings obtained indicate that there were sites on the ship with IAQ issues relating to high levels of CO_2 and HCHO, low temperature, high RH, and low ventilation rate (air movement). These issues need to be rectified in order to ensure good indoor environmental quality for the crew members of the ship. The other IAQ parameters investigated were in compliance with the acceptable levels set by DOSH (2010).

The results presented in this study are based on observations, sampling and testing of environmental quality parameters within the ship at the specified times, on the day of the test. The level of contaminants may differ depending on the level of activity within the assessed sites. Hence, in order to improve the IAQ on the ship, it is proposed that continuous monitoring and measurements of the IAQ parameters be conducted.

REFERENCES

American Bureau of Shipping (ABS) (2001). *Guide for Crew Habitability on Ships*. American Bureau of Shipping (ABS), Houston, Texas.

Brightman, H.S. & Moss, N. (2000). Sick building syndrome studies and the compilation of normative and comparative values. *In* Spengler, J.D., Samet, J.M. & McCarthy, J.F. (Eds.), *Indoor Air Quality Handbook*. McGraw Hill, New York, pp. 3.1-3.32.

Chan, L.Y., Lau, W.L., Wang, X.M. & Tang, J.H. (2003). Preliminary measurements of aromatic VOCs in public transportation modes in Guangzhou, China. *Environ. Int.*, **29**: 429– 435.

Chien, Y.C. (2007). Variations in amounts and potential sources of volatile organic chemicals in new cars. *Sci. Total Environ.*, **382**: 228–239.

Department of Occupational Safety & Health (DOSH) (2010). *Industry Code of Practice of Indoor Air Quality 2010*. Department of Occupational Safety and Health (DOSH), Ministry of Human Resources, Malaysia.

Elsafty, A. F. (2010). Ventilation efficiency inside a ship's cabin based on air diffusion performance index (ADPI). *Eur. J. Sci. Res.*, **40**: 102 -114.

Environmental Protection Agency (EPA) (1998). *Building Air Quality: A Guide for Building Owners and Facility Managers*. Environmental Protection Agency (EPA), Washington DC.

Jang, M.S., Koh, C.D. & Moon, I.S. (2007). Review of thermal comfort design based on PMV / PPV in cabins of Korean maritime patrol vessels. *Build Environ.,* **42**: 55-61.

Kadiyala, A. & Kumar, A. (2011). Study of in-vehicle pollutant variation in public transport buses operating on alternative fuels in the city of Toledo, Ohio. *Open Environ. Biol. Monit. J.*, **4**: 1-20.

Korea Research Institute of Ships and Ocean Engineering (KRISO) (2002). *Study on Occupational Fatigue in Patrol Vessels*. Korea Research Institute of Ships and Ocean Engineering (KRISO), Daejeon.

Lau, W.L. & Chan, L.Y. (2003). Commuter exposure to aromatic VOCs in public transportation modes in Hong Kong. *Sci. Total Environ.,* **308**: 143–155.

Mahdi, C.I. & Zalini, Y. (2010). An evaluation of indoor air quality (IAQ) in a machinery room of a floating vessel. *Journal Defence Secur.*,**1**: 258 – 274.

Sun, S.K. & Yun, G.L. (2010). Field measurements of indoor air pollutant concentrations on two new ships. *Build. Environ.*, **45**: 2141-2147.

Sundell, J. (2004). On the history of indoor air quality and health. *Indoor Air*, **14**: 51-58.

Sustainable Energy Authority (SEA) (2012). *Air Movement*. Sustainable Energy Authority (SEA), Victoria.

Webster, A.D. (1997). *The Contribution of Ventilation System Design and Maintenance to Air Quality in Passenger Ships*. The Institute of Marine Engineers, London.

Wolkoff, P. & Kjægaard, S.K. (2007). The dichotomy of relative humidity on indoor air quality. *Environ. Int.*, **33**: 850-857.

Webster, A.D. & Reynolds, G.L. (2005). Indoor air quality on passenger ships. *In* Pluschke, P. (Ed.), *The Handbook of Environmental Chemistry: Air Pollution-Part H, Vol. 4*, Springer, New York, pp. 335-349.

EVALUATION OF THE EFFECT OF VARYING GLOBAL POSITIONING SYSTEM (GPS) SIGNAL POWER LEVELS ON GPS ACCURACY

Dinesh Sathyamoorthy*, Mohd Faudzi Muhammad, Rafidah Malik & Nor Irza Shakhira Bakthir, Siti Robiah Abdul, Shalini Shafii, Aliah Ismail, Lim Bak Tiang, Zainal Fitry M Amin, Mohd Rizal Ahmad Kamal, Siti Zainun Ali and Mohd Hasrol Hisam M Yusoff

Instrumentation and Electronics Technology Division (BTIE), Science & Technology Research Institute for Defence (STRIDE), Ministry of Defence, Malaysia

*E-mail: dinesh.sathyamoorthy@stride.gov.my

ABSTRACT

In this study, Global Positioning System (GPS) simulation is used to evaluate the effect of varying GPS signal power levels on the accuracy of two handheld GPS receivers; Garmin GPSmap 60CSx (evaluated GPS receiver) and Garmin GPSmap 60CS (reference GPS receiver). Both receivers employ the GPS L1 coarse acquisition (C/A) signal. With decreasing GPS signal power level, probable error values increase due to decreasing carrier-to-noise density (C/N_0) levels for GPS satellites tracked by the receiver. Varying probable error patterns are observed for readings taken at different locations and times. This is due to the GPS satellite constellation being dynamic, causing varying GPS satellite geometry over location and time, resulting in GPS accuracy being location / time dependent. For all the readings taken, the evaluated GPS receiver recorded lower probable error values as compared to the reference GPS receiver. This occurred as the evaluated GPS receiver has higher receiver sensitivity, and hence, is able to obtain lower position dilution of precision (PDOP) values. In addition, it has lower receiver noise, reducing the value of its user equivalent ranging error (UERE).

Keywords: *Global Positioning System (GPS) simulation; GPS signal power level; probable error; receiver sensitivity; satellite geometry.*

1. INTRODUCTION

There is a steady growth in the entrenchment of Global Navigation Satellite Systems (GNSS) in current and upcoming markets, having penetrated various consumer

products, such as cell phones, personal navigation devices (PNDs), cameras and assimilation with radio-frequency identification (RFID) tags, for various applications, including navigation, surveying, timing reference and location based services (LBS). While the Global Positioning System (GPS), operated by the US Air Force (USAF), is the primarily used GNSS system worldwide, the upcoming Galileo and Compass systems, and the imminent conversion of *Global'naya Navigatsionnaya Sputnikovaya Sistema* (GLONASS) signals from frequency division multiple access (FDMA) to code division multiple access (CDMA) look set to make multi-satellite GNSS configurations the positioning, navigation & timing (PNT) standard for the future.

However, many GNSS users are still not fully aware of the vulnerabilities of GNSS systems to various error parameters, such as ionospheric and tropospheric delays, satellite clock, ephemeris and multipath errors, satellite positioning and geometry, and signal interferences and obstructions. These error parameters can severely affect the accuracy of GNSS readings, and in a number of cases, disrupt GNSS signals (Volpe, 2001; Harding, 2001; Kaplan & Hegarty, 2006; IDA, 2009; GAO, 2009; Dinesh, 2009, 2011; Last, 2010; Schwartz, 2010; Gibbons, 2010; McNeff, 2010; RAE, 2011; Schue, 2012).

To this end, many designers are working on improving characteristics of GNSS receivers, such as lower power consumption, the tracking of weak satellite signals, faster acquisition times and more accurate position fixes. At present, many developers and users still struggle to identify suitable standard tests to objectively verify and evaluate the functionality and performance of GNSS receivers. Commonly tested parameters in GNSS receiver evaluations include time to first fix (TTFF), warm start time to first fix (WTFF), reacquisition time, timing accuracy, static positioning accuracy, receiver sensitivity and radio frequency interference (RFI) operability (ION, 1997; Aloi *et al.*, 2007; Dinesh *et al.*, 2009a; Petrovski *et al.*, 2010).

GNSS receiver evaluations conducted by the Science & Technology Research Institute for Defence (STRIDE), including recent tests focusing on RFI operability (Dinesh *et al.*, 2009b, 2010a, b), has thus employed only field evaluations. Such field evaluations are subject to various error parameters which are uncontrollable by users. Furthermore, field evaluations are not suitable for accurate measurements of GNSS receiver performance parameters as (Aloi *et al.*, 2007; Dinesh *et al.*, 2009a, Petrovski *et al.*, 2010; Kou & Zhang, 2011):

i. These parameters should be measured under conditions in which the various errors are user-controlled and repeatable.

ii. Field evaluations are also subject to unintended signal interference from radio, radar, etc., and unwanted signal multipath and obscurations.

iii. Field evaluations cannot be employed to measure receiver sensitivity, as this requires precise measurements of GNSS signals.

The ideal GNSS receiver evaluation methodology would be using a GNSS simulator which can be used to generate multi-satellite GNSS configurations, transmit GNSS signals which simulate real world scenarios, and adjust the various error parameters. This would allow for the evaluations of GNSS receiver performance under various repeatable conditions, as defined by users. As the evaluations are conducted in controlled laboratory environments, they will be inhibited by unwanted signal interferences and obstructions (Aloi *et al.*, 2007; Dinesh *et al.*, 2009a; Petrovski *et al.*, 2010; Kou & Zhang, 2011).

In this study, GPS simulation is used to evaluate the effect of varying GPS signal power levels on the accuracy of two handheld GPS receivers; Garmin GPSmap 60CSx (Garmin, 2007) (evaluated GPS receiver) and Garmin GPSmap 60CS (Garmin, 2004) (reference GPS receiver). Both receivers employ the GPS L1 coarse acquisition (C/A) signal. The simulated GPS signals are generated using an Aeroflex GPSG-1000 GPS simulator (Aeroflex, 2010), which was procured by STRIDE for the Tenth Malaysian Plan (RMK10) project entitled *Evaluation of the Effect of Radio Frequency Interference (RFI) on Global Positioning System (GPS) Signals via GPS Simulation*.

2. METHODOLOGY

The study was conducted in the STRIDE semi-anechoic chamber (A. Faridz *et al.*, 2010) using the test setup shown in Figure 1. The following assumptions were made for the tests:

i. No ionospheric or troposheric delays
ii. Zero clock and ephemeris error
iii. No multipath fading or unintended obstructions
iv. No unintended interference signals.

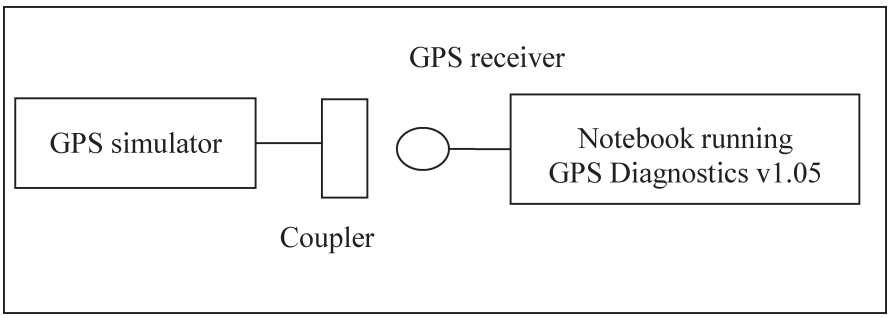

Figure 1: The test setup employed.

The date of simulation was set at 10 January 2012. The almanac data for the period was downloaded from the US Coast Guard's web site (USCG, 2011), and imported

into the GPS simulator. For each GPS receiver, the test procedure was conducted for coordinated universal time (UTC) times of 0000, 0300, 0600 and 0900 for the following coordinates:

i. N 2° 58’ E 101° 48’ (Kajang, Selangor, Malaysia)
ii. N 39° 45’ W 105° 00’ (Denver, Colorado, USA)
iii. S 16° 55’ E 145° 46’ (Cairns, Queensland, Australia)
iv. S 51° 37’ W 69° 12’ (Rio Gallegos, Argentina).

The Trimble Planning software (Trimble, 2009) was used to estimate GPS satellite coverage at the test areas for the period of the tests (Figure 2).

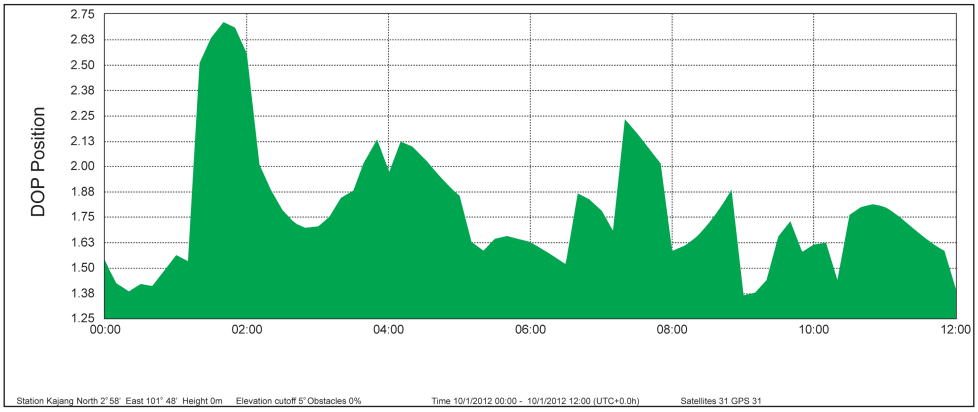

(a)

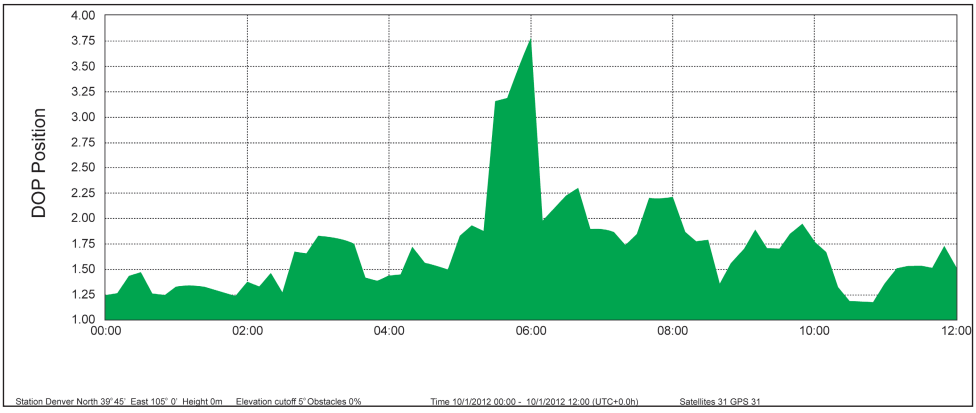

(b)

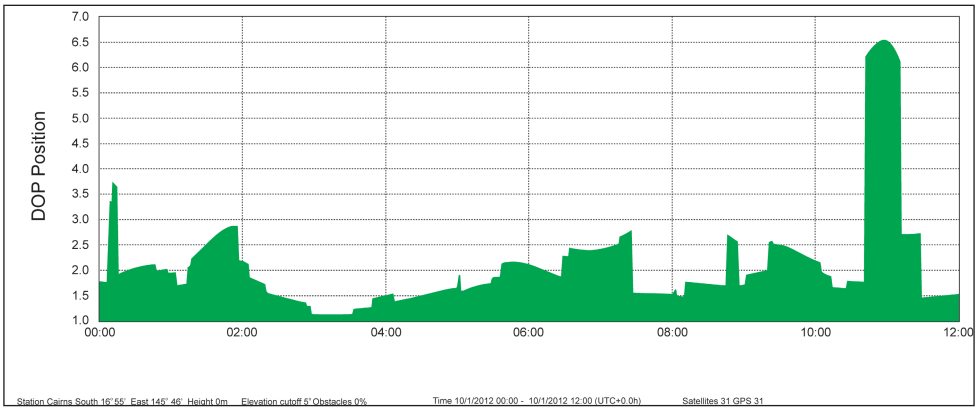

(c)

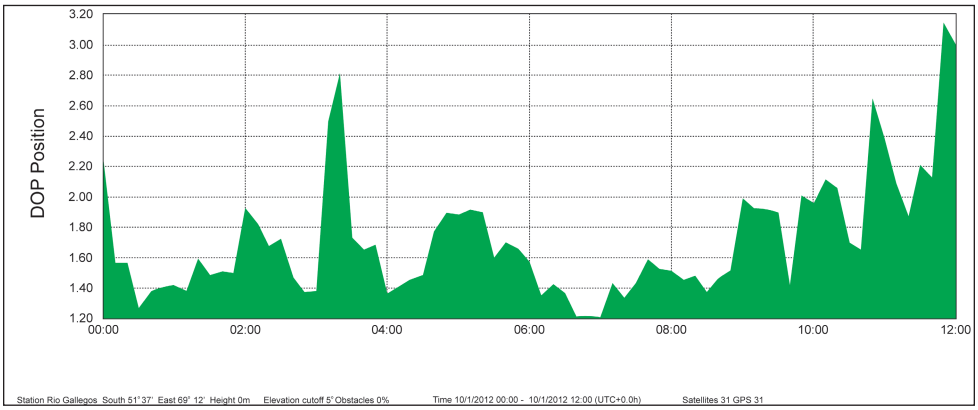

(d)

Figure 2: Position dilution of precision (PDOP) of GPS coverage at the test areas for the period of the tests: (a) Kajang; (b) Denver; (c) Cairns; and (d) Rio Gallegos. (Source: Screen captures from the Trimble Planning software)

Transmission was started at GPS signal power level of -131 dBm and reduced to -155 dBm at decrements of 3 dBm. At each power level, GPS Diagnostics v1.05 (CNET, 2004) was used to record the values of horizontal probable error (HPE), vertical probable error (VPE) and estimate probable error (EPE).

3. RESULTS AND DISCUSSION

The recorded probable error values for the tests are shown in Figures 3-14. With decreasing GPS signal power level, probable error values increase due to decreasing carrier-to-noise density (C/N_0) levels for GPS satellites tracked by the receiver, which is the ratio of received GPS signal power level to noise density. Lower C/N_0 levels result in increased data bit error rate when extracting navigation data from GPS signals, and hence, increased carrier and code tracking loop jitter. This, in turn, results in more noisy range measurements and thus, less precise positioning (DOD, 2001; USACE, 2003; Kaplan & Hegarty, 2006; Petovello, 2009).

For all the readings taken, the evaluated GPS receiver recorded lower probable error values as compared to the reference GPS receiver. This occurred as the evaluated GPS receiver has higher receiver sensitivity, and hence, is able to obtain lower PDOP values. In addition, it has lower receiver noise, reducing the value of its user equivalent ranging error (UERE), which is the total expected magnitude of position errors due to measurement uncertainties from the various error components for a particular receiver. It is observed that in cases of high PDOP values, the difference of probable errors between the two receivers is much smaller (e.g., Denver at 0600, Cairns at 0000 and Rio Gallegos at 0300).

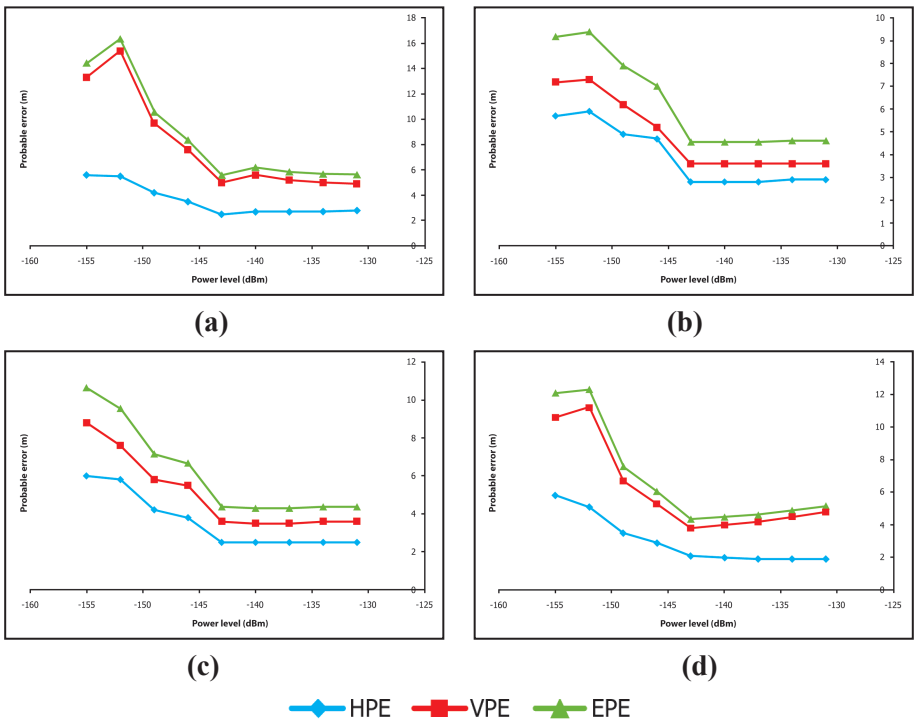

Figure 3: Recorded probable error values for the evaluated GPS receiver at Kajang for UTC times of: (a) 0000; (b) 0300; (c) 0600; and (d) 0900.

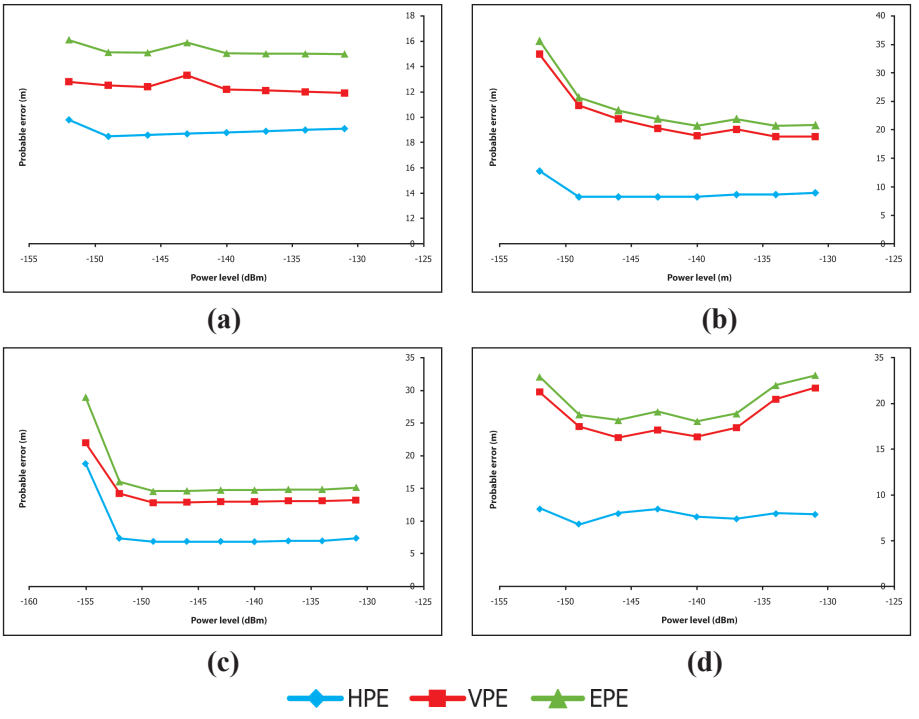

Figure 4: Recorded probable error values for the reference GPS receiver at Kajang for UTC times of: (a) 0000; (b) 0300; (c) 0600; and (d) 0900.

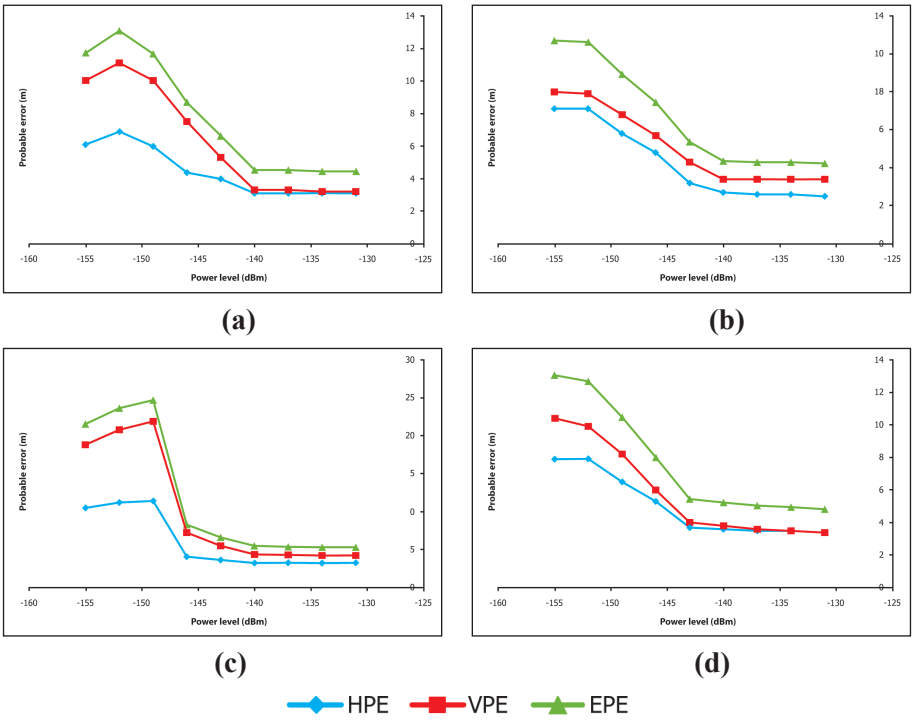

Figure 5: Recorded probable error values for the evaluated GPS receiver at Denver for UTC times of: (a) 0000; (b) 0300; (c) 0600; and (d) 0900.

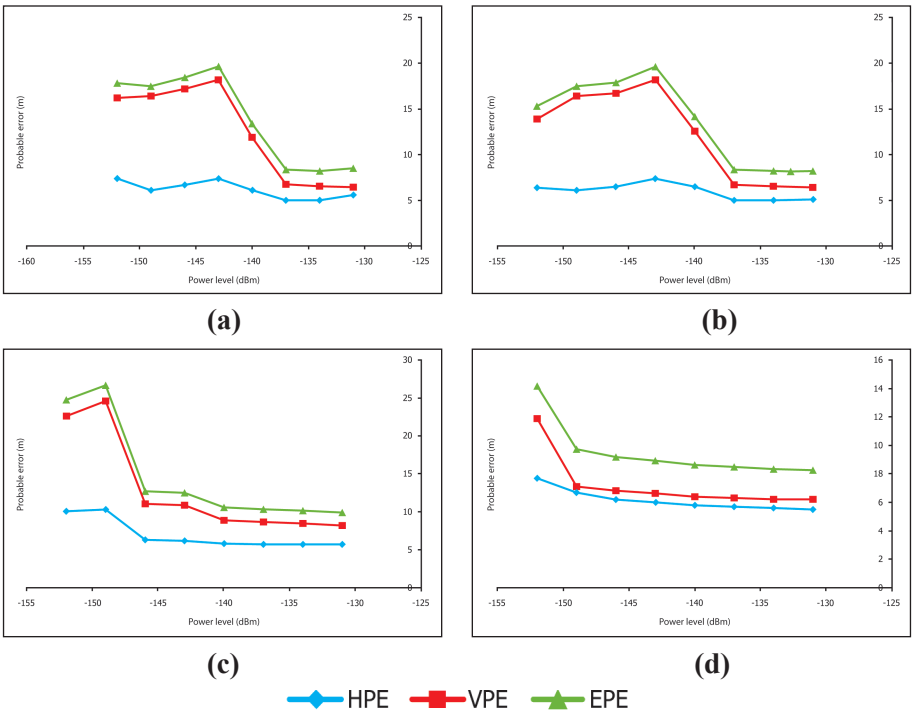

Figure 6: Recorded probable error values for the reference GPS receiver at Denver for UTC times of: (a) 0000; (b) 0300; (c) 0600; and (d) 0900.

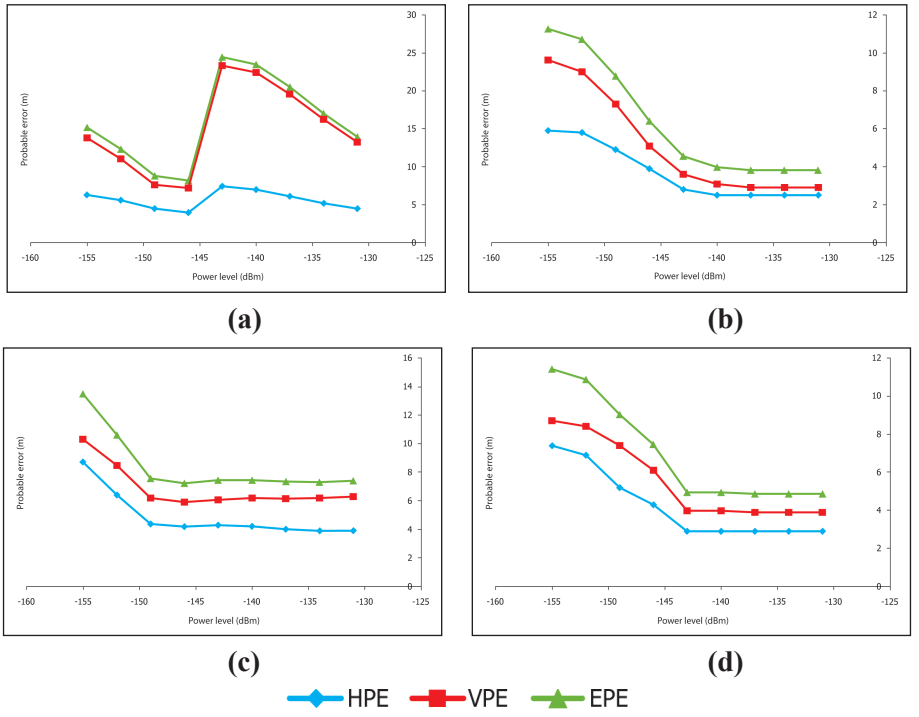

Figure 7: Recorded probable error values for the evaluated GPS receiver at Cairns for UTC times of: (a) 0000; (b) 0300; (c) 0600; and (d) 0900.

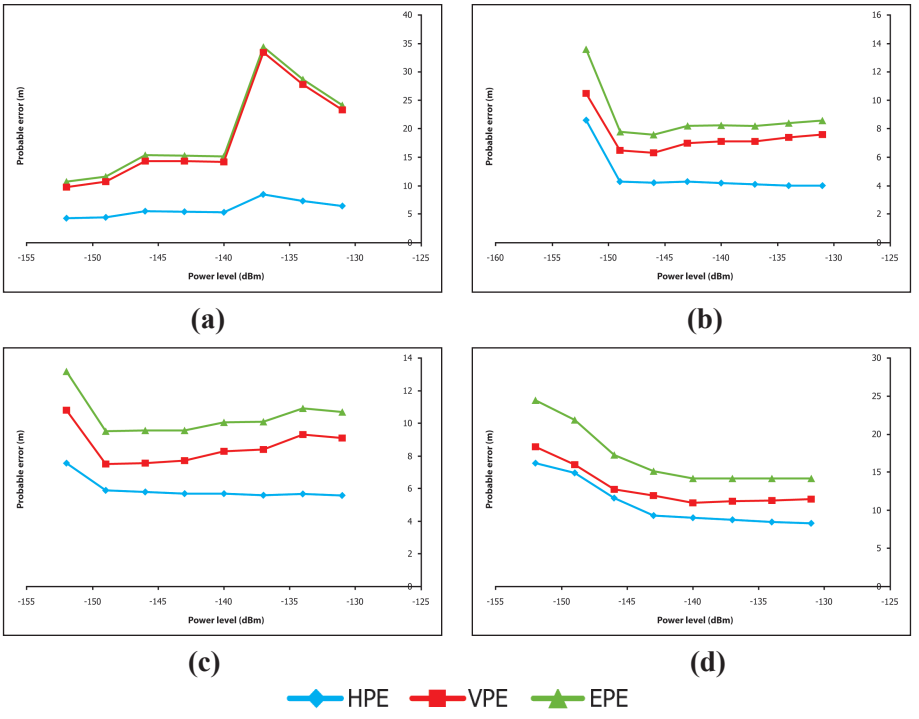

Figure 8: Recorded probable error values for the reference GPS receiver at Cairns for UTC times of: (a) 0000; (b) 0300; (c) 0600; and (d) 0900.

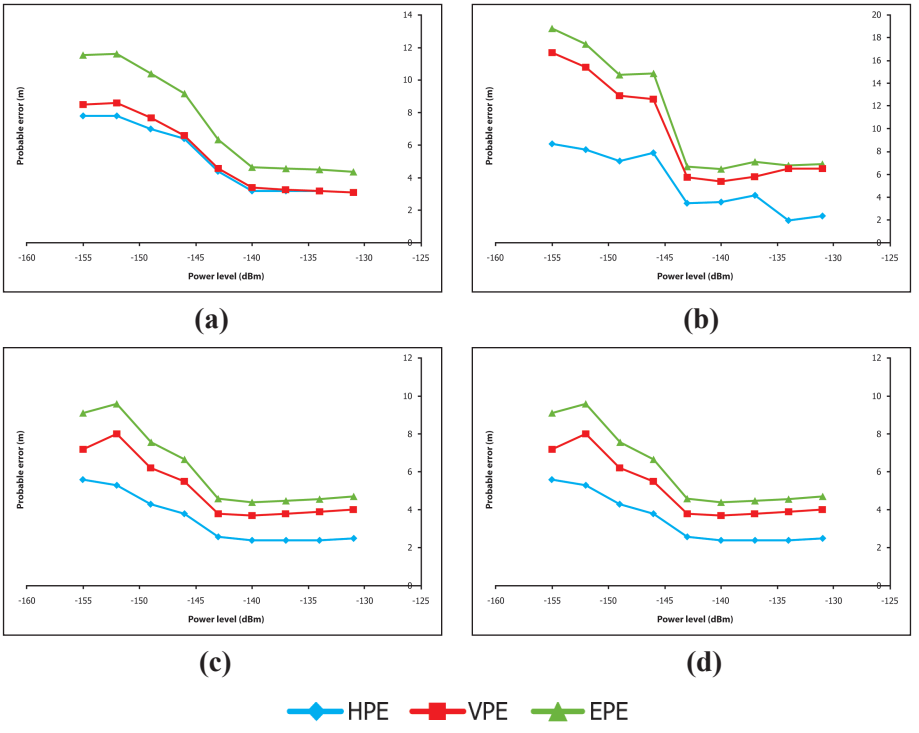

Figure 9: Recorded probable error values for the evaluated GPS receiver at Rio Gallegos for UTC times of: (a) 0000; (b) 0300; (c) 0600; and (d) 0900.

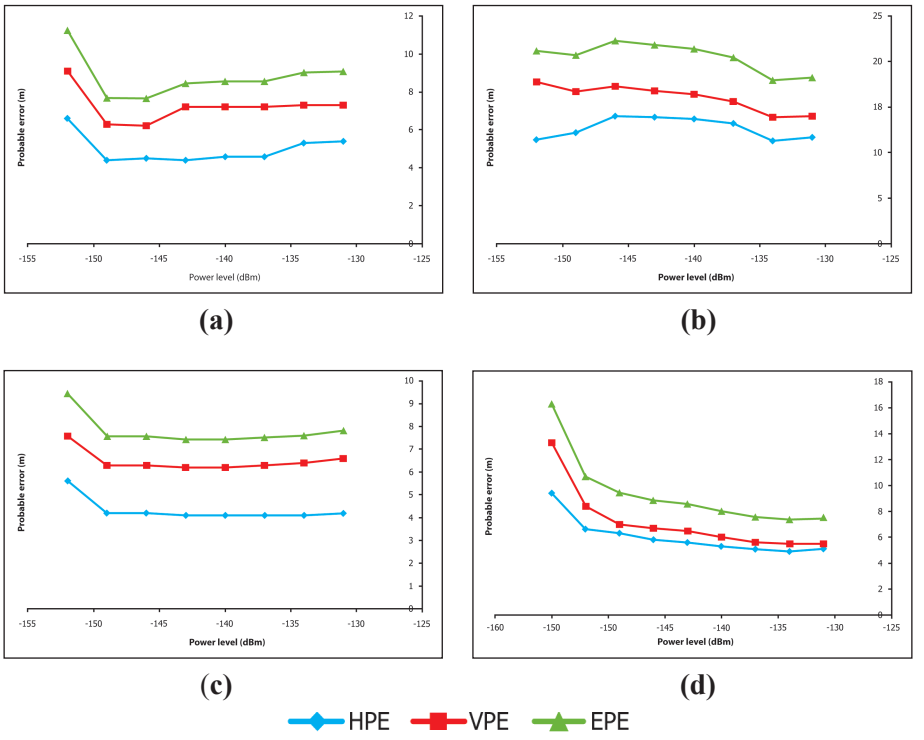

Figure 10: Recorded probable error values for the reference GPS receiver at Rio Gallegos for UTC times of: (a) 0000; (b) 0300; (c) 0600; and (d) 0900.

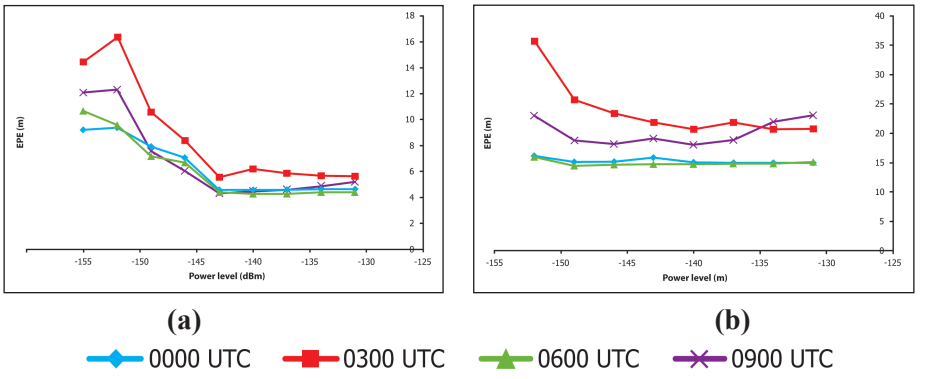

Figure 11: Comparison of recorded EPE values of varying times at Kajang for the (a) evaluated; and (b) reference GPS receivers.

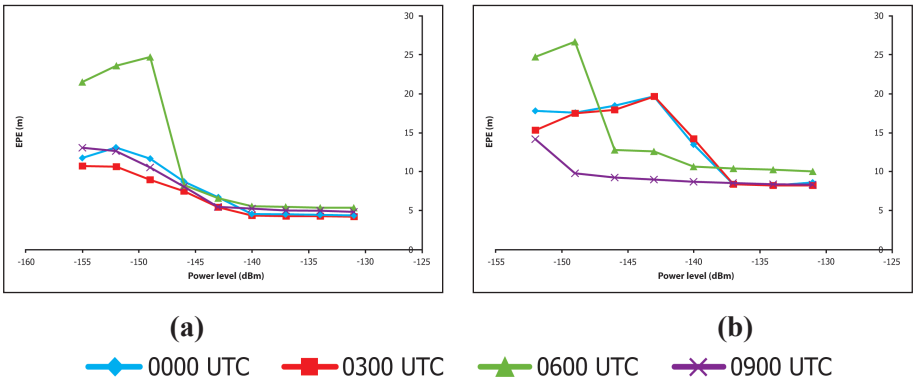

Figure 12: Comparison of recorded EPE values of varying times at Denver for the (a) evaluated; and (b) reference GPS receivers.

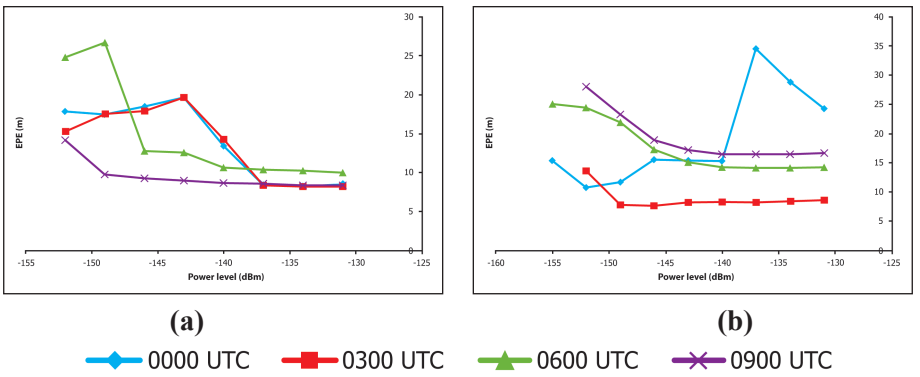

Figure 13: Comparison of recorded EPE values of varying times at Cairns for the (a) evaluated; and (b) reference GPS receivers.

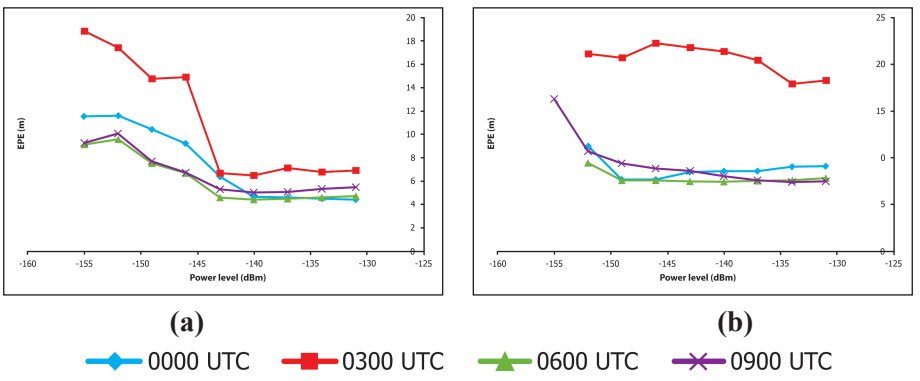

Figure 14: Comparison of recorded EPE values of varying times at Rio Gallegos for the (a) evaluated; and (b) reference GPS receivers.

Varying probable error patterns are observed for the each of the readings. This is due to the GPS satellite constellation being dynamic, causing varying GPS satellite geometry over location and time, resulting in GPS accuracy being location / time dependent (DOD, 2001; USACE, 2003; Kaplan & Hegarty, 2006; Huihui *et al.*, 2008; Dinesh *et al.*, 2010b). In general, the highest probable error values were observed for readings with the highest PDOP values (Kajang at 0300, Denver at 0600, Cairns at 0000 and Rio Gallegos at 0300), while the lowest probable error values were observed for readings with the lowest PDOP values (Kajang at 0000 and 0600, Denver at 0300, Cairns at 0300 and Rio Gallegos at 0600). The reading taken at 0900 at Kajang corresponds with a period where PDOP values improve significantly, resulting in probable error values initially decreasing, before increasing due to reduction in GPS signal power level. The reading taken at 0000 at Cairns corresponds with a period where PDOP values increase and decrease significantly in a short period of time, resulting in probable error values initially increasing and then decreasing, bucking the trend of the other readings.

It is observed that for all the readings, the values of VPE are larger than HPE, as GPS receivers can only track satellites above the horizon, resulting in GPS height solution being less precise than the horizontal solution (DOD, 2001; USACE, 2003; Kaplan & Hegarty, 2006; Huihui *et al.*, 2008; Dinesh *et al.*, 2010b). The difference between VPE and HPE values is significantly larger for the reference GPS receiver as compared to the evaluated GPS receiver. The reference GPS receiver, having lower receiver sensitivity, has much better horizontal component accuracy as compared to the vertical component. For the GPS evaluated receiver, with higher receiver sensitivity, while the horizontal component accuracy is still larger, the difference with the vertical component is much smaller.

4. CONCLUSION

With decreasing GPS signal power level, probable error values increase due to decreasing C/N_0 levels for GPS satellites tracked by the receiver. Varying probable error patterns are observed for readings taken at different locations and times. This is due to the GPS satellite constellation being dynamic, causing varying GPS satellite geometry over location and time, resulting in GPS accuracy being location / time dependent. For all the readings taken, the evaluated GPS receiver recorded lower probable error values as compared to the reference GPS receiver. This occurred as the evaluated GPS receiver has higher receiver sensitivity, and hence, is able to obtain lower PDOP values. In addition, it has lower receiver noise, reducing the value of its UERE.

ACKNOWLEDGEMENT

The authors are grateful to Mr. Kamarulzaman Mustapa, Mr. Ahmad Faridz Abd. Ghafar, Mr. Khairul Anwar Abd Rahim for their support. The authors would like to thank Datuk Dr. Abdul Ghaffar Ramli, Director-General, Science & Technology Research Institute for Defence (STRIDE), Ministry of Defence, Malaysia, Mdm. Wan Salwa Wan Hassan, Director of the STRIDE Instrumentation & Electronics Division (BTIE), and the reviewers, Dr. Mahdi Che Isa and Mdm. Halijah Ahmad, for their suggestions that helped strengthen this manuscript.

REFERENCES

A. Faridz, A.G., M. Razali, M. Y. & W. Salwa, W.H. (2010). STRIDE's 3 meters EMC semi-anechoic chamber: Design considerations and compliance to standards. *2010 IEEE Asia-Pacific Conference on Applied Electromagnetics (APACE 2010)*, 9-11 November 2010, Tiara Beach Resort, Port Dickson, Negeri Sembilan.

Aeroflex (2010). *Avionics GPSG-1000 GPS / Galileo Portable Positional Simulator*. Aeroflex Inc., Plainview, New York.

Aloi, D.N., Alsliety, M. & Akos, D.M. (2011). A methodology for the evaluation of a GPS receiver performance in telematics applications. *IEEE T. Instrum. Meas.*, **56**: 11-24.

CNET (2004). *GPSDiag 1.0*. Available online at:

http://download.cnet.com/GPSDiag/3000-2130_4-4951103.html (Last access date: 31 January 2010).

Department of Defence (DOD) (2001). *Global Positioning System Standard Positioning Service Performance Standard. Command, Control, Communications, and Intelligence*. Department of Defence (DOD), Washington D.C.

Dinesh, S. (2009). Vulnerabilities of civilian Global Navigation Satellite Systems (GNSS) signals: A review. *Defence S&T Tech. Bull.*, **2**: 100-114.

Dinesh, S. (2011). Vulnerabilities of Global Navigation Satellite Systems (GNSS) signals to jamming and spoofing. *GIS Day 2011*, 17 March 2011, Universiti Putra Malaysia (UPM), Serdang, Selangor.

Dinesh , S., Wan Mustafa, W.H., Mohd Faudzi., M., Kamarulzaman, M., Nor Irza Shakhira, B., Siti Robiah, A., Norhayaty, Z., Aliah, I., Lim, B.T., Arumugam, P., Zainal Fitry, M.A., Mohd. Rizal, A.K., Azlina, B. & Mohd. Hasrol, H.M.Y. (2009a). The advantages of Global Navigation Satellite Systems (GNSS) receiver evaluation using GNSS simulators. *BUDI*, **2009**: 6-10.

Dinesh , S., Wan Mustafa, W.H., Mohd Faudzi., M., Kamarulzaman, M., Nor Irza Shakhira, B., Siti Robiah, A., Norhayaty, Z., Aliah, I., Lim, B.T., Arumugam, P., Zainal Fitry, M.A., Mohd. Rizal, A.K., Azlina, B. & Mohd. Hasrol, H.M.Y. (2009b). Evaluation of the effect of radio frequency interference (RFI) on Global Positioning System (GPS) receivers. *Defence S&T Tech. Bull.*, **2**: 115-129.

Dinesh , S., Wan Mustafa, W.H., Mohd Faudzi., M., Kamarulzaman, M., Hasniza, H., Nor Irza Shakhira, B., Siti Robiah, A., Shalini, S., Jamilah, J., Aliah, I., Lim, B.T., Zainal Fitry, M.A., Mohd. Rizal, A.K., Azlina, B. & Mohd. Hasrol, H.M.Y. (2010a). Evaluation of power levels required by interference signals at various distances to jam the Global Positioning System (GPS) L1 coarse acquisition (C/A) signal. *Defence S&T Tech. Bull.*, **3**: 14-28.

Dinesh , S., Wan Mustafa, W.H., Mohd Faudzi., M., Kamarulzaman, M., Hasniza, H., Nor Irza Shakhira, B., Siti Robiah, A., Shalini, S., Jamilah, J., Aliah, I., Lim, B.T., Zainal Fitry, M.A., Mohd. Rizal, A.K., Azlina, B. & Mohd. Hasrol, H.M.Y. (2010b). Evaluation of the effect of radio frequency interference (RFI) on Global Positioning System (GPS) accuracy. *Defence S&T Tech. Bull.*, **3**: 100-118.

Garmin (2004). *GPSmap 60CS Owner's Manual*. Garmin International Inc., Olathe, Kansas.

Garmin (2007). *GPSmap 60CSx Owner's Manual*. Garmin International Inc., Olathe, Kansas.

Government Accountability Office (GAO) (2009). *Global Positioning System: Significant Challenges in Sustaining and Upgrading Widely Used Capabilities*. Report to the Subcommittee on National Security and Foreign Affairs, Committee on Oversight and Government Reform, House of Representatives, Government Accountability Office (GAO), U.S.

Harding, S.J. (2001). *Vulnerability Assessment of the Transport Infrastructure Relying on the Global Positioning System*. QinetiQ Group, Buckingham Gate, London.

Huihui, W., Xingqun, Z. & Yanhua, Z. (2008). Geometric dilution of precision for GPS single-point positioning based on four satellites. *J. Syst. Eng. Electr.*, **19**: 1058-1063.

Institute for Defense Analyses (IDA) (2009). *Independent Assessment Team (IAT): Summary of Initial Findings on eLoran*. Institute for Defense Analyses (IDA), Alexandria, Virginia.

Institute of Navigation (ION) (1997). *Institute of Navigation Standard 101 (ION STD 101): Recommended Test Procedures for GPS Receivers, Revision C*. Institute of Navigation (ION), Manassas, Virginia.

Kaplan, E.D. & Hegarty, C.J. (2006). *Understanding GPS: Principles and Applications*. Artech House, Norwood, Massachusetts.

Kou, Y. & Zhang, H. (2011). Verification testing of a multi-GNSS RF signal Simulator. *Inside GNSS*, **5**: 52-61.

Last, D. (2010). GNSS: The present imperfect. *Inside GNSS*, **5**: 60-64.

McNeff, J. (2010). Changing the game changer: The way ahead for military PNT. *Inside GNSS*, **5**: 44-51.

Petovello, M. (2009). Carrier-to-noise density and AI for INS / GPS integration. *Inside GNSS*, **4**: 20-29.

Petrovski, I., Townsend, B. & Ebinuma, T. (2010). Testing multi-GNSS equipment: Systems, simulators and the production pyramid. *Inside GNSS*, **5**: 52-61.

Royal Academy of Engineering (RAE) (2011). *Global Navigation Space Systems: Reliance and Vulnerabilities*. Royal Academy of Engineering, London.

Schue, C. (2012). The challenges of realizing a global navigation capability. *ION International Technical Meeting (ITM) 2012*, 30 January - 1 February 2012, Newport Beach, California.

Schwartz, N. (2010). The United States as an aerospace nation: Challenges and opportunities. *Tuft University Institute for Foreign Policy Analysis (IFPA) Fletcher Conference on National Security Strategy and Policy*, 20-21 January 2010, The Ronald Reagan Building and International Trade Center, Washington, D.C.

Trimble (2009). *Trimble's Planning Software*. Available online at:

http://www.trimble.com/planningsoftware.shtml (Last access date: 17 November 2009).

US Army Corps of Engineers (USACE) (2003). *NAVSTAR Global Positioning System Surveying. Engineer Manual*. EM 1110-1-1003, US Army Corps of Engineers (USACE), Washington D.C.

US Coast Guard (USCG) (2011). *GPS NANUs, Almanacs, & Ops Advisories*. Available online at:

http://www.navcen.uscg.gov/?pageName=gpsAlmanacs (Last access date: 6 January 2012).

Volpe (2001). *Vulnerability Assessment of the Transport Infrastructure Relying on the Global Positioning System*. John A. Volpe National Transportation Systems Center, Department of Transport, Washington D.C.

COMPARISON OF SOFTWARE FOR RESCUE OPERATION PLANNING DURING AN ACCIDENT IN A NUCLEAR POWER PLANT

Andrea Malizia[*1], Ivan Lupelli[1], Fabrizio D'Amico[1], Alessandro Sassolini[1], Andrea Fiduccia[2], Anna Maria Quarta[1], Roberto Fiorito[3], Antonio Gucciardino[1], Maria Richetta[1], Carlo Bellecci[1] & Pasquale Gaudio[1]

[1]Department of Industrial Engineering, Faculty of Engineering, University of Rome "Tor Vergata", Italy
[2]Intergraph Italia LLC, Italy
[3]Department of Surgery, Faculty of Medicine and Surgery, University of Rome "Tor Vergata", Italy

[*]E-mail: malizia@ing.uniroma2.it

ABSTRACT

This work has been developed to determine proper analytical support instruments in order to improve emergency operation systems in case of accidents in a nuclear reactor. The case study analysed is in reference to an experimental nuclear fission power plant in Italy (the information about the name and location of this plant has been omitted for safety reasons). The accidental event's consequences were simulated using a free licensed software, HotSpot, and the results obtained were compared with the results obtained using ISPRA Software, the only software certified by the Italian National Institute for Environmental Protection and Research (ISPRA) for nuclear accidents. Once the reliability of HotSpot was established, the most critical incident for this reactor, as indicated by the latest revision of the National Plan on Protective Measures against Nuclear and Radiological Emergencies, was simulated. The simulation results (for areas classified with respect to limits on effective dose) were used as input in the development, through the use of the GeoMedia GIS software, of a vulnerability model that takes into account the spatial distribution of the population in the area affected by the event. In the context of emergency management, such instruments should be integrated with the systems of command & control centres for crisis management and the emergency operation centre (EOC), and made available to the entire chain of emergency management, including the field teams with handheld terminals.

Keywords: *Radiological emergency planning; ISPRA Software; HotSpot; nuclear power plant accident scenario; ground deposition.*

1. INTRODUCTION

Emergency systems planning is extremely important in order to mitigate the effects of a disaster. Proper identification of risks scenarios and information in terms of people and resources involved are fundamental for safety and security reasons (Giaimo, 2000). In addition, the quantification of possible releases of radioactive material and the scheduling of these data are necessary to start actions and countermeasures that are to be taken in order to minimise the impact on the environment and health.

Referring to nuclear emergencies, the Italian Legislative Decree No. 230/95 provides that the Department of Civil Protection (DCP), Prime Minister's Office, sign a National Emergency Plan to deal with emergencies arising from other countries. The same law requires for the prefects in the areas involved to have appropriate action plans, known as External Emergency Plans (EEP) in case of accidents at nuclear facilities in Italy. Internal Emergency Plans (IEP) are intended to identify actions to be taken by officers of the involved accident site, in case of emergency (Bomboni *et al.*, 2007).

The guidelines of DCP for external emergency planning for major accidents and hazards at nuclear installations require the establishment of three zones (Murray, 1993):

i. High impact zone: Immediately near the nuclear power plant, characterised by high lethality level for people.

ii. Damage zone: Characterised by severe and irreversible damage for people who do not take proper measures for self-protection.

iii. Attention zone: Characterised by not serious damage but critical for psychological consequences.

This work has been developed to determine proper analytical support instruments in order to improve emergency operation systems in case of accidents in a nuclear reactor. The case study analysed is in reference to an experimental nuclear fission power plant in Italy (the information about the name and location of this plant has been omitted for safety reasons). The accidental event's consequences were simulated using a free licensed software, HotSpot, and the results obtained were compared with the results obtained using ISPRA Software, the only software certified by the Italian National Institute for Environmental Protection and Research (ISPRA) for nuclear accidents. This study is aimed at determining HotSpot's suitability as a viable alternative for radiological emergency planning by evaluating its ability to produce results that are comparable with ISPRA Software.

2. SOFTWARE EVALUATED

2.1 ISPRA Software

In a nuclear/radiological accident scenario, it is important to have very quick and accurate data on the incident's impact on the surrounding area. This includes quantities such as absorbed dose, external radiation and ground contamination. In light of these considerations, ISPRA Software provides that, at the time of the emergency, the user can select an accidental event previously defined, calculated and graphically developed (incident based), and make changes to the input data in order to have a simulated event comparable with the real event. Once the type of incident has been identified, using the parameters that the system requires, the output is provided in the form of graphs and radioactivity deposition isopleth maps.

The isopleth curves are plotted with reference to a system of axes with the origin coincident with the nuclear installation, the *x*-axis coincident with the direction of the wind, the *y*-axis perpendicular to the *x*-axis, and the *z*-axis coincident with the vertical plane of the nuclear plant. The graphs in the output are used to identify radiometric contamination (Homann, 2009).

2.2 HotSpot

HotSpot, which is available on the website of the National Atmospheric Release Advisory Center (NARAC) (NARAC, 2011), is able to provide quick approximation of the effects of radioactive substance release into the environment. In order to increase the effectiveness of the evaluation of incidents, HotSpot includes atmospheric dispersion models which are differentiated by explosion, fire or resuspension of plutonium, uranium or tritium. The general models are those used for the mix of radionuclides or other radionuclides. These models estimate the radiological impact due to the release of radioactive materials for short time periods (hours). In addition to the atmospheric dispersion models, HotSpot offers three subprograms:

i. Nuclear explosion: To evaluate the consequences of a nuclear explosion.

ii. Field instrument for detection of low-energy radiation (FIDLER): To calibrate instruments for ground-survey measurements of plutonium and provide initial screening for possible plutonium uptake in the lungs. The FIDLER program can also be applied to any instrument suitable for measuring external radiation levels and non-plutonium mixtures.

iii. Radionuclides in the workplace: To evaluate the dose of exposure for workers at risk.

The mathematical model used for the code is a Gaussian type, which is able to reproduce the emission behaviour of a virtual radiological source starting from the appropriate boundary conditions. In order to better assess the radiological effects near the drop zone, the same virtual source is used to model the initial atmospheric distribution of radiation following an accidental event (Homann, 2009). For evaluation of radiological scenarios, HotSpot uses the methods of radiation dosimetry recommended by the International Commission on Radiological Protection (ICRP) (ICRP, 2005) and the US Environmental Protection Agency's (EPA) Federal Guidance Reports No. 11, 12 and 13 (EPA, 1988, 1993, 1999).

3. CASE STUDY

3.1 Simulated Scenario

For the evaluation of the consequences of an accidental event in the reference site, the release of a set of radionuclides from a fireplace is simulated. For this case study, the release will only cover radionuclide I131. In order to analyse this scenario, ISPRA Software incident based system, known as System - C (release from a fireplace), is used, while the HotSpot subroutine that allows this assessment is "General Plume".

3.2 Results

For this study, the two software are compared in terms of the ground deposition. The boundary conditions used to define the case study with HotSpot are as shown in Table 1. The simulation was implemented using T = 240 min as the starting time. A comparison of the results obtained by the software is shown in Table 2, where the elapsed time decreases with distance in order to have a computational time delay that is acceptable.

From the results obtained, it is deduced that the two software are comparable for distance of not exceeding 1 km from the point of release. At distance of 0.2 km, the percentage of variation between the ground deposition values for both software is approximately 25%. This variation decreases with increasing distance until a minimum value of 3% is reached at distance of 0.6 km. Moving from this distance, HotSpot begins to be more conservative than ISPRA Software, providing larger ground deposition values. The variation between the two software increases to 85% at distance of 1 km.

Table 1: Boundary conditions used to define the case study with HotSpot.

Parameter	Value
Source material	I-131 8.04 d
Material at risk	3.7 x 10^{10} Bq
Damage ratio	1,000
Leakpath factor	1,000
Airborne fraction	1,000
Respirable fraction	1,000
Respirable release fraction	1,000
Effective release height	20.00 m
Wind speed (*h*=10 m)	2.00 m/s
Distance coordinates	All distances are on the "Plume Centerline"
Wind speed (*h=H-eff*)	2.14 m/s
Stability class	C
Respirable deposition velocity	0.30 cm/s
Non-respirable deposition velocity	0 cm/s
Receptor height	1.5 m
Inversion layer height	None
Sample time	0.010 min
Breathing rate	3.33 x 10^{-4} m^3/sec
Inner contour dose	1.00 x 10^{-7} Sv
Middle contour dose	5.00 x 10^{-8}Sv
Outer contour dose	1.00 x 10^{-8} Sv

Beyond this distance, the two software are not comparable, with the differences being significant, by an order of magnitude at distance of 1.5 km, two orders at 2 km, five orders at 3 km and seven orders at 5 km. This marked difference in response to distances greater than 1 km is justified by the basic settings of the two software. As shown in Figure 1, the trend of ground deposition values generated by ISPRA Software tends to decrease linearly for distance of up to 1 km, after which the values tend to move more quickly to zero.

Table 2: Comparison of ground deposition results obtained using the two software.

Distance from point of release (km)	Elapsed time (min)	Ground deposition (Bq/m^2)		Delta (%)
		ISPRA Software	HotSpot	
0.1	238	$2.12x10^5$	$2.40x10^5$	13.21
0.2	236	$7.42x10^4$	$5.50x10^4$	-25.88
0.3	234	$3.18x10^4$	$2.30x10^4$	-27.67
0.4	232	$1.56x10^4$	$1.30x10^4$	-16.67
0.5	230	$9.02x10^3$	$8.00x10^3$	-11.31
0.6	228	$5.33x10^3$	$5.50x10^3$	3.19
0.7	226	$3.41x10^3$	$4.10x10^3$	20.23
0.8	224	$2.22x10^3$	$3.10x10^3$	39.64
0.9	222	$1.51x10^3$	$2.50x10^3$	65.56
1.0	220	$1.08x10^3$	$2.00x10^3$	85.19
1.5	210	$1.96x10^2$	$9.10x10^3$	-
2.0	200	$5.12x10^1$	$5.30x10^3$	-
3.0	180	$8.41x10^0$	$9.1x10^5$	-
5.0	140	$6.47x10^{-1}$	$9.1x10^6$	-

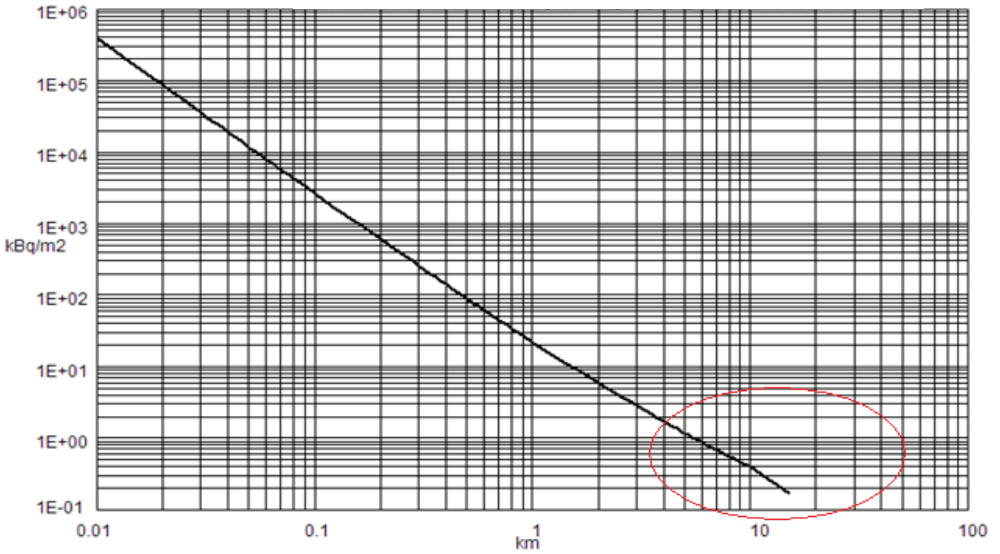

Figure 1: Trend of ground deposition values generated by ISPRA SOFTWARE for the case study.

3.3 Discussion

From the results of the case study, the HotSpot's output is comparable with that of ISPRA Software for distance of up to 1 km from the point of release. Based on this, it can be concluded that HotSpot is a viable alternative to the ISPRA SOFTWARE for radiological emergency planning for the first km, while for larger distances, it is better to use ISPRA Software11.

ISPRA Software was specifically designed to simulate nuclear power plant accident scenarios. Hence, its code was to be modelled based on real scenarios, which are processed by the system. On the other hand, HotSpot uses generic base scenarios, allowing the user to change a wide range of parameters that can have consequences on the evaluation of characteristic variables of the event (Homann, 2009).

In regards to the data in output, a limitation found when using ISPRA SOFTWARE is that there are difficulties in its graphical user interface (GUI). This is certainly a critical factor in emergency management, as the output data from the system is not real, but rather, must be further manipulated to get a picture of the real situation.

Regarding the update of the libraries of the two software, HotSpot's library is constantly updated automatically with the latest X-ray doses and methods of conversion, and these libraries are available on the internet. Updating of ISPRA SOFTWARE libraries needs to be conducted by typing manually from the different sources.

In order to ensure proper implementation of the algorithms, HotSpot automatically launches a review of the software, so that every module is compared with a series of cases in its database to verify the correct functionality. Each default scenario is simulated and its results are compared with the results documented. This ensures that the software is properly installed and that all algorithms are operational.

4. INTEGRATION WITH GEOMEDIA FOR RESPONSE OPTIMISATION

Once HotSpot's simulated scenarios were validated with reference to the current EEP Test Site, the most critical incident for this reactor as defined by the latest revision of National Plan on Protective Measures against Nuclear and Radiological Emergencies (DCP, 2010) is simulated. The results obtained with this simulation are then processed with Intergraph Corp's GeoMedia GIS software, which is used to demarcate territorial zonings of the risks linked to demographic factors, drawing on data accessible via spatial data infrastructure (SDI). This is used to identify a model of vulnerability for the area in question, taking into account the real distribution of the population in the territory.

A further step in ensuring good emergency planning is to provide an update of the data contained in the EEP, which was last revised in the year 2000. Several significant differences were found between the data in the EEP and SDI. The most significant difference is related to demographic data, for which there was an increase in the population at an average rate of 42.5% in the area surrounding the test site for up to a distance of 5 km. In addition, demographic analysis was performed for up to a distance of 10 km from the centre (Figure 2). The road infrastructure network was also analysed to ensure proper identification of the roads to be used for emergencies and proposals for new ones.

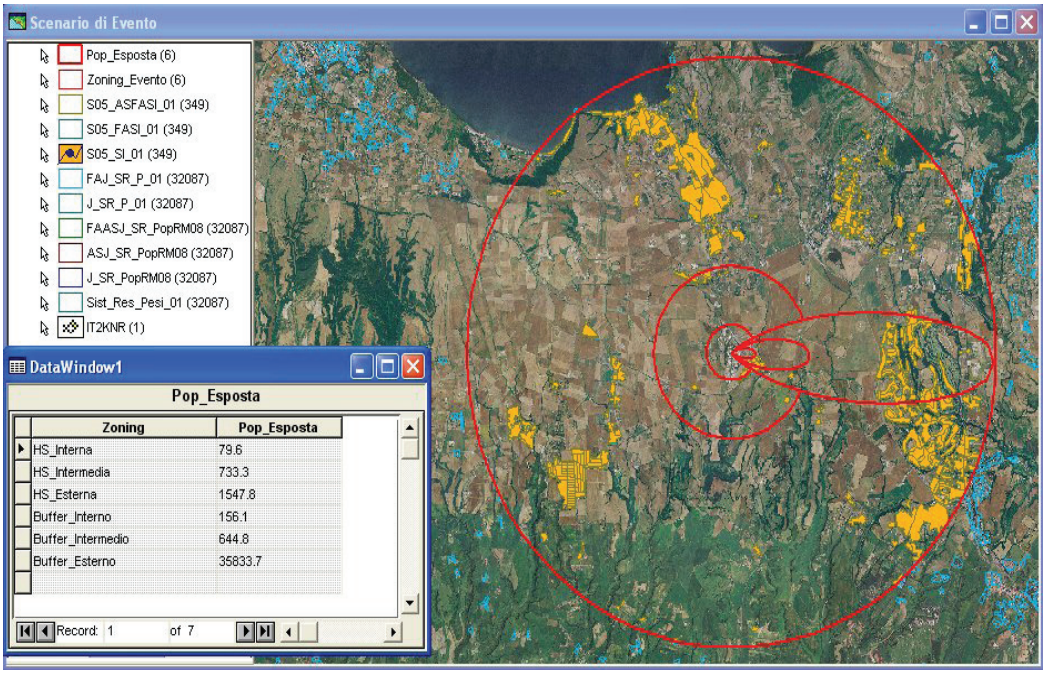

Figure 2: HotSpot analysis results presented on a GeoMedia map.

As shown in Figure 3, using dynamic queries cascade (piping) and the functional attributes of GeoMedia, the calculation of risk zoning is updated near-real-time via the calculation of scenarios using HotSpot with changing meteorological parameters. This update is then automatically propagated to the common operational picture (COP) through GeoMedia's web-services.

With reference to nuclear risks, and the technical apparatus and organisation envisaged by the Italian national regulations, the proposed system can ensure that users have updated, highly interoperable maps. This can allow for increased efficiency in coordinating inter-agency transactions between the control centre (provided by the IEP), DCP and other agencies responsible for emergency management. It also provides the ability to increase situational awareness for the teams in the field with handheld terminals.

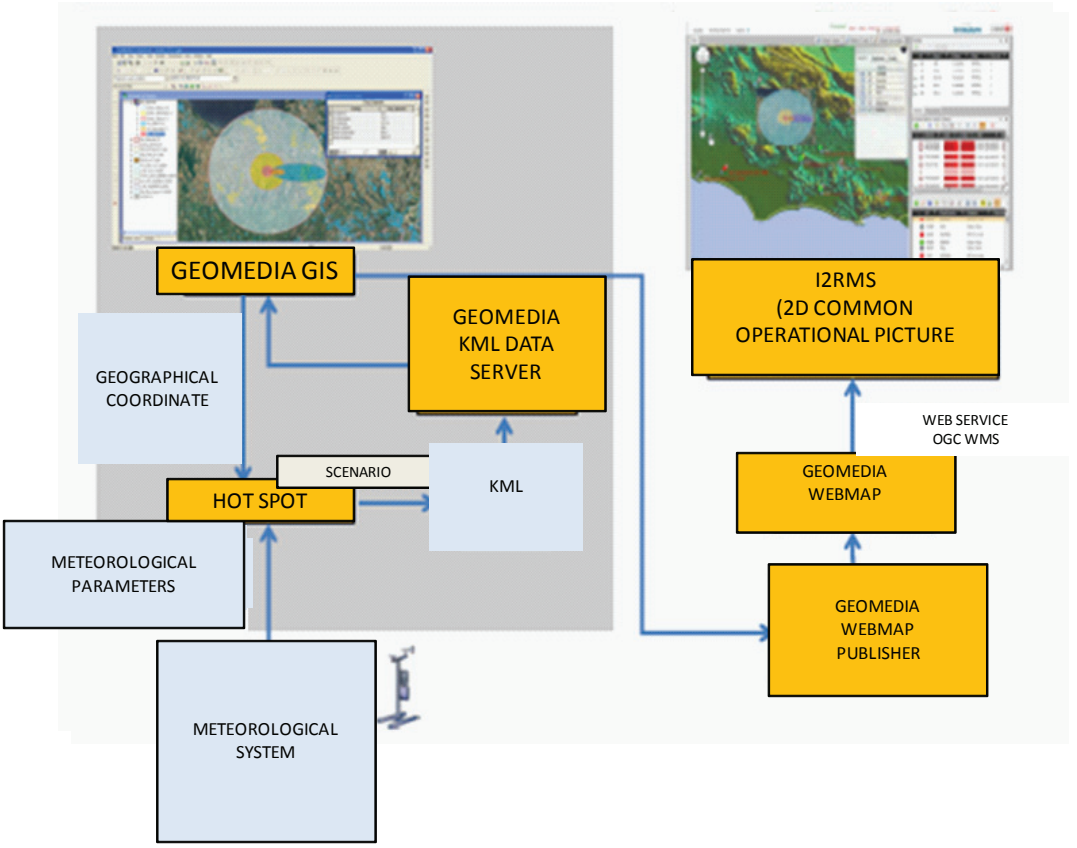

Figure 3: Integration of HotSpot with GeoMedia's geoworkspace for near-real-time calculation of scenarios and risk zoning, and updating to the COP.

5. CONCLUSION

The use of HotSpot as an alternative to ISPRA Software has highlighted a number of advantages such as being "free license", ease of use and wide variety of simulated scenarios. While it has an inaccurate definition of results at large distances in cases of dispersion and ground deposition scenarios, it does provide advantages in terms of a large variety of options for defining a scenario, clear and detailed visualisation of results, updating of radioprotection limits, self-verification of operations, and integration with GIS. Based on this, it can be concluded that HotSpot is a good alternative to ISPRA Software for radiological emergency planning.

ACKNOWLEDGMENT

The authors would like to thank Prof. Pasquale Gaudio for offering the opportunity to develop this work, and for the constant ability to coordinate groups of scientists and experts in the sector of CBRN risk.

REFERENCES

Bomboni, E., Cerullo, N., Lomanaco, G. & Romanello, V. (2007). *Note Sulla Sicurezza Nucleare*. Università Degli Studi di Pisa, Pisa.

Department of Civil Protection (DCP) (2010). *National Plan on Protective Measures against Nuclear and Radiological Emergencies*. Prime Minister's Office, Rome.

Environmental Protection Agency (EPA) (1988). *Federal Guidance Report No. 11: Limiting Values Radionuclide Intake and Air Concentration, and Dose Conversion Factors for Inhalation, Submersion, and Ingestion*. Environmental Protection Agency (EPA), Washington DC.

Environmental Protection Agency (EPA) (1993). *Federal Guidance Report No. 12: External Exposure to Radionuclides in Air, Water, and Soil*. Environmental Protection Agency (EPA), Washington DC.

Environmental Protection Agency (EPA) (1999). *Federal Guidance Report No. 13: Cancer Risk Coefficients for Environmental Exposure to Radionuclides*. Environmental Protection Agency (EPA), Washington DC.

Giaimo, G. (2000). Il rischio nucleare in Italia. *DPC Informa*, **23**: 19-24.

Homann, S.G. (2009). *HotSpot: Health Physics Codes Version 2.07*. National Atmospheric Release Advisory Center (NARAC), Livermore, California.

International Commission on Radiological Protection (ICRP) (2005). *Basis for Dosimetric Quantities Used in Radiological Protection*. International Commission on Radiological Protection (ICRP), Ottawa, Ontario.

Murray, R.L. (1993). *Nuclear Energy, 4th Edition*. Pergamon Press, Oxford.

National Atmospheric Release Advisory Center (NARAC) (2011). HotSpot: Health Physics Codes for the PC. Available online at: https://narac.llnl.gov/HotSpot/HotSpot.html (Last access date: 14 March 2012).

APPLICATION OF A QUALITATIVE MODEL FOR EVALUATION OF EXPECTED RISK IN AN URBAN CRISIS: CASE STUDY ON ROME

Valentina Sabato[1*] & Roberto Mugavero[2]

[1]Observatory on Security and CBRNe Defence, Italy
[2] Department of Electronic Engineering, Faculty of Engineering, University of Rome "Tor Vergata", Italy

[*]Email: v.sabato@osdife.it

ABSTRACT

The assessment of expected damage following a natural or man-made urban crisis must take into account the integration and interaction of different aspects; social, economic, cultural and political. However, the estimation of all these elements simultaneously is difficult to conduct with traditional mathematical models because they are linear. Therefore, in this study, in order to estimate the potential damage caused by a particular catastrophic event, we use an alternative methodological approach; a qualitative model. This method is able to provide a measure of the risk index of the territory from the presence and consistency of certain factors that are important to assess the area's vulnerability. The multi-criteria decision making (MCDM) method, Analytic Hierarchy Process (AHP), allows us to determinate the cost / benefit ratio of any problem where the advantages and disadvantages cannot be considered only in economic terms. For this reason, AHP enables us to analyse complex environmental problems with qualitative data, and quantify the natural and anthropic risk indices. It is demonstrated that densely populated metropolises, such as Rome, are equally exposed to both natural and man-made events, and hence, anthropic risks should not be neglected.

Keywords: *Urban risk; natural and anthropic risk indices; Analytic Hierarchy Process (AHP); systemic vulnerability; potential damages.*

1. INTRODUCTION

Modern urban systems are, on a daily basis, exposed to a considerable number of risks which threaten the physical / spatial and anthropic / functional dimensions. We can divide these risks into two macro-areas; natural and anthropic. In order to calculate the probability of occurrence of a natural event, there is a wide range of scientific literature and established mathematical relationships that link the risks to vulnerability and exposure (Ragheb, 2011). On the contrary, we do not have

sufficient tools to calculate the probability of a man-made event. In fact, in this type of events, a set of dynamic elements that are linked by interactive relationships come into play, so it is virtually impossible to define the potential risks and exposure levels of the territory. Hence, we can consider an anthropic risk as "multiple risks". It is a phenomenon generated by a various human activities that interact in synergy with each other in the same place. These events can have direct or indirect impacts, and can involve parts of or the entire city at different levels.
While the anthropogenic component has considerable influence on risk assessment, the exposure level is generally made to coincide with the assessment of natural hazards. This happens because anthropic risk is spread out over time, and human settlements and migration processes make it harder to perceive the dangers of human activities. For this reason, emergency planners often underestimate man-made risks. To this end, we can define a new concept of risk; urban risk. It is the sum of the components of risks that result from natural events and anthropogenic factors. The formalisation of this risk is not straightforward because it is composed of many disparate elements, and appropriate mathematical models to evaluate the connections between these elements have yet to be developed.

It is clear that traditional linear numerical models may not be able to properly assess the level risk of a city. Therefore, we have tested the application of a multi-criteria decision making (MCDM) model; Analytic Hierarchy Process (AHP) (Saaty, 1996; Falcone *el al.*, 2009). AHP is generally used to evaluate and verify the quality of complex production systems that are employed in industries. It allows users to consider simultaneously both the constitutive elements and their connections. In this way, we can estimate and quantify the weight that every element has on the proper functioning of the analysed system. As AHP allows us to decompose and then rationally recompose any type of complex system, it can provide valuable support to the new approach of assessing urban risk.

For the study, we have chosen the city of Rome as it is a multi-ethnic metropolis and has a central role in Italy's administration. In fact, Rome is an evident example of the complex processes and large number of elements that contribute to the stability of the city and country. Initially, we conducted a risk analysis and then, calculated the natural I_{Rn} and anthropic I_{Ra} risk indices for each of the areas that are included in the territory of Rome. Using AHP, it is demonstrated that, anthropic risks cannot be underestimated, as they affect the stability of the city just as much as, if not more than, natural risks.

2. RISK ASSESSMENT: SYSTEMIC VULNERABILITY

The United Nations Disaster Relief Office (UNDRO) defines risk in an area as the product of hazard, vulnerability and exposure (UNDRO, 1979). Generally, risk analysis uses linear mathematical models to establish the probability of occurrence

of a disaster in a particular place. With these models and some experimental data, the event intensity can also be calculated. In order to compute the risk degree R_{ij} related to item *i* during a disaster *j*, the following relationship is used:

$$R_{ij} = H_j \cdot V_j \cdot E_j \quad (1)$$

where:

i. hazard H_{ij} is the probability that an event will occur at a certain time and in a particular place

ii. vulnerability V_{ij} is the capacity that a system has to deal with the stress produced by a natural or anthropic event

iii. exposure E_j is the number of human, economic and social elements that are exposed to hazard.

The evolutionary trend of urban systems has resulted in the classification of various categories of vulnerabilities in order to effectively respond to crisis events. These categories are:

i. Direct vulnerability: the transition from punctual crisis to system crisis

ii. Induced vulnerability: the collapse of a single element generates the crisis of the entire system

iii. Temporary vulnerability: the loss of efficiency in crisis

iv. Dynamic vulnerability: the loss of efficiency in the recovery time

v. Deferred vulnerability: the ensemble of social and economic crises that occur in post-emergency.

The potential damages, resulting from a disaster, are very different and hence, traditional computational models can only describe them partially. Therefore, it is very important to fully understand the analysed system to reduce the gap between expected and real damages. Damages can be classified as follows:

i. Physical damage: occurs in the impact phase and causes damages to persons and property

ii. Systemic-organisation damage: occurs in the rescue and emergency phases, and are usually caused by inefficiency of services, shortage of rescue and trained personnel, and inadequate rescue

iii. Process damage: Occurs in the reconstruction and normality recovery phases, and represents damages which are spatially and temporally more diffuse and heterogeneous.

Obviously, these damages are related to the complexity of the urban system, and they have impact on economic, social, political and administrative aspects.

The linear analytical approach (Ragheb, 2011) does not take into account the connections that exist between the organisational, economic and social elements of a country, even though these elements are essential to correctly describe an urban / regional situation. City vulnerability cannot be assessed by considering separately each risk as the effects of a disaster involve an area that extends beyond the zone which is directly affected by the event (Figure 1).

Systemic vulnerability is related not only to the interactions that exist between the explained item and the reference context, but also to the connections that exist between adjacent elements and their links with induced, temporary and deferred effects. This necessarily requires a qualitative and quantitative approach which must also be able to consider aspects (social, economic, cultural and political) that are not normally regarded (Mugavero & Sabato, 2011).

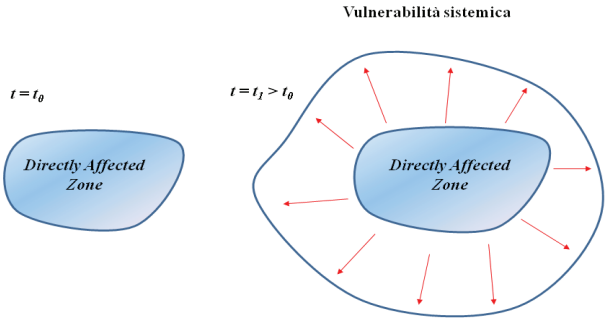

Figure 1: Systemic vulnerability of a zone which is directly affected by an event; t_0 indicates the time of occurrence of the event, while t_1 indicates a period after the occurrence of the event (Adapted from Torre *et al.*, 2005).

3. THE RISK ASSESSMENT MODEL

In order to build a suitable risk assessment model, the interactions between the respective risk factors should be taken into account to estimate the weight of each effect on the maximum total damage. The total potential damage D_{ij} caused by a particular catastrophic event can be computed using the following equation:

$$D_{ij} = R_j \cdot K_i = \sum_j H_j \cdot V_j \cdot E_j \cdot K_i \qquad (2)$$

where K_i is the recovery cost.
If a K_i-valued asset is exposed to different events, D_{ij} is computed as follows:

$$D_{ij} = R_j \cdot K_i = \sum_j H_j \cdot V_j \cdot K_i \; D_{ij} = R_{R_{ij}} \cdot K_i = \sum_j P_{ij} \cdot \sum_j V_{ij} \cdot K_j \qquad (3)$$

H_{ij} and V_{ij} are equal to 1 when the maximum damage occurs. In this case, we have the complete loss of exposed assets.

With this model, we can qualitatively and quantitatively standardise all vulnerability factors, and build complementarity relationships that are defined as the weight of every factor on the overall vulnerability. To implement this model, we must first divide the system into a set of elements that need to be organised hierarchically. At the top of the hierarchical pyramid, there are more aggregated elements while at the bottom there are more disaggregated elements. AHP is able to analyse each sub-element individually and then, quantify the system by analysing the connections between the parts (Saaty, 1996).

Decision makers must attribute a weight to each element of the hierarchy, whereby the weight is referred to the main goal, which is a function of the weights of all subordinate elements that belong to the hierarchy. Generally, the model consists of three decomposition levels, namely categories, factors and indicators (Figure 2). The category is the first maximum decomposition of the system, factors are all aspects of the same category, and finally, indicators are measurable characteristics of the factors. The AHP method uses Saaty's scale to assign the weight in terms of the evaluation levels shown in Table 1.

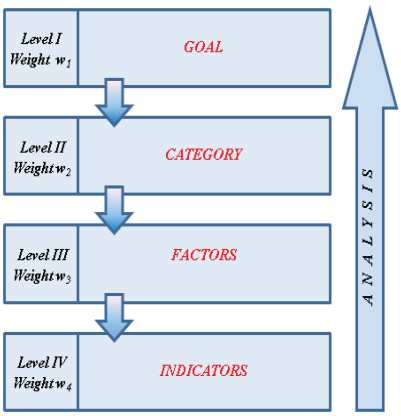

Figure 2: The hierarchical structure used in AHP.
(Adapted from Torre *et al.*, 2005)

Table 1: Saaty's scale for determining weights of elements in the hierarchy.
(Adapted from Saaty, 1996)

Quantitative relation	Semantics
9	Extremely more important
7	Much more important
5	More important
3	Moderately more important
1	Equally important
1/3	Moderately less important
1/5	Less important
1/7	Much less important
1/9	Extremely less important

Saaty's method involves the standardisation of quality levels using the method of comparing elements in pairs. $A_1, A_2, A_3, \ldots, A_n$ are a set of n elements that belong to a generic level of a hierarchical structure, while $W_1, W_2, W_3, \ldots, W_n$ are the corresponding weights, and $a_{ij} = w_i/w_j$ is the weight of element i with respect to element j. Using all these elements, we can construct the pairwise comparison square matrix A (Table 2), which has rank equal to n, and it is reciprocal and positive.

Table 2: The pairwise comparison matrix A. (Adapted from Torre *et al.*, 2005)

	A_1	A_2	A_3	...	A_n
A_1	a_{11}	a_{12}	a_{13}	…	a_{1n}
A_2	a_{21}	a_{22}	a_{23}	…	a_{2n}
A_3	a_{31}	a_{32}	a_{33}	…	a_{3n}
…	…	…	…	…	...
A_n	a_{n1}	a_{n2}	a_{n3}	…	a_{nn}

The matrix elements have the following properties:

- $a_{ii} = 1$ (symmetry property)
- $a_{ij} > 0$ (axiom of positivity)
- $a_{ij} = 1/a_{ji}$ (property of reciprocity)
- $a_{ik}=a_{ij}a_{jk}$ (property of consistency)

Based on these properties, only half of the matrix needs to be compiled because the elements which are located below the main diagonal are the reciprocals of the elements which are above the diagonal. All elements of this diagonal have total weight equal to 1.

In this way, we have constructed a matrix which is generally not consistent and therefore, a consistency coefficient must be considered to allow us to assess the consistency of the matrix, and, if necessary, build a new one. The matrix allows us to derive the priority order of the elements, i.e., the priority scale is a vector of cardinal values that express the priority among compared elements. This vector coincides with the main eigenvector of the matrix of weights.

To extract this vector, we have to solve the general problem of eigenvalues:

$$(A - \lambda) \cdot p = \lambda_{\max} \cdot p \tag{4}$$

where:
$p = (p_1, p_2, p_3, \ldots, p_n)^T$: eigenvector and
λ_{max}: maximum eigenvalue.

AHP simultaneously calculates the eigenvectors and the principal eigenvalue for checking the internal consistency of A. This test is very important because humans have a recognised limitation in simultaneously building logical relationships between

many objects and concepts. We identify the degree of tolerable inconsistency using the consistency index *CI*:

$$CI = \frac{\lambda_{\max} - n}{n - 1} \tag{5}$$

where the degree of inconsistency is equal to the percentage of deviation of λ_{max} from the *n.* CI is used to compute the consistency ratio *CR* using the following equation:

$$CR = CI / RI \tag{6}$$

where the average random consistency *RI* is obtained from a sample of 500 reciprocal square arrays which have dimensions of $n = 1, 2, 3, \ldots, 10$ (Table 4). If *CR* is less than 20%, the matrix is considered to be consistent. Otherwise, we must proceed with a revaluation of the matrix.

Table 4 : Determination of average random consistency *RI* based on rank matrix *n*. (Adapted from Fanizzi & Misceo, 2010)

Rank matrix *n*	Average random consistency *RI*
1	--
2	0
3	0.512
4	0.89
5	1.11
6	1.25
7	1.35
8	1.40
9	1.45
10	1.49

4. CASE STUDY: ROME

The territory of Rome is huge, and hence, we decided that in order to conduct the multi-criteria analysis, it was necessary to divide the area into several subzones. Since Rome is divided into 32 quarters (Figure 3(a)), we adhered to this subdivision, and then, we calculated I_{Rn} and I_{Ra} for each quarter. Later, we conducted a census of all the relevant structures of the city, in regards to the administration of Italy (Mugavero & Sabato, 2011). We realised that most of these facilities are located in the Centro Storico quarter. For this reason, we calculated the two indices for each district in Centro Storico (Figure 3(b)).

Using the goals of computing anthropic and natural risk indices (Level I), the corresponding categories for each goal (Level II), and the factors of population and settlement (Level III), the hierarchical tree shown in Figure 4 was prepared. The indicators used for each factor (Level IV) are as shown in Figure 5.

The settlements were divided according to their functions:

i. Architectural value: monuments, archaeological sites, museums, historical buildings, etc.

ii. Residential: residential buildings

iii. Productive: industries, storage facilities and other plants that are subject to relevant industrial risk.

iv. Welfare: hospitals, medical clinics, rescue units, police stations, etc.

v. Administration: ministries, town halls, public offices, consulates, etc.

vi. Social: stadium, cinemas, shopping centres, sport clubs, theatres, churches, etc.

(a)

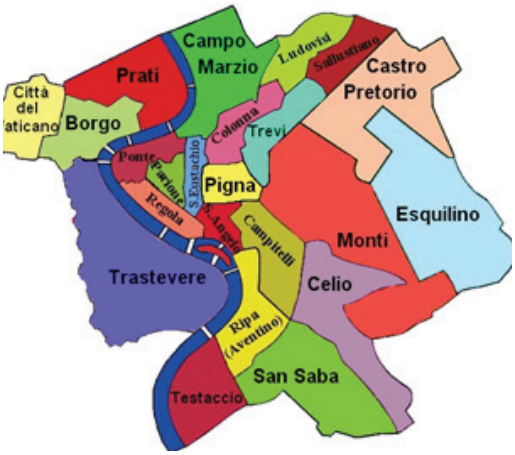

(b)

Figure 3: (a) The quarters of Rome; and (b) The districts of Centro Storico. (Source: Roma Capitale, 2012)

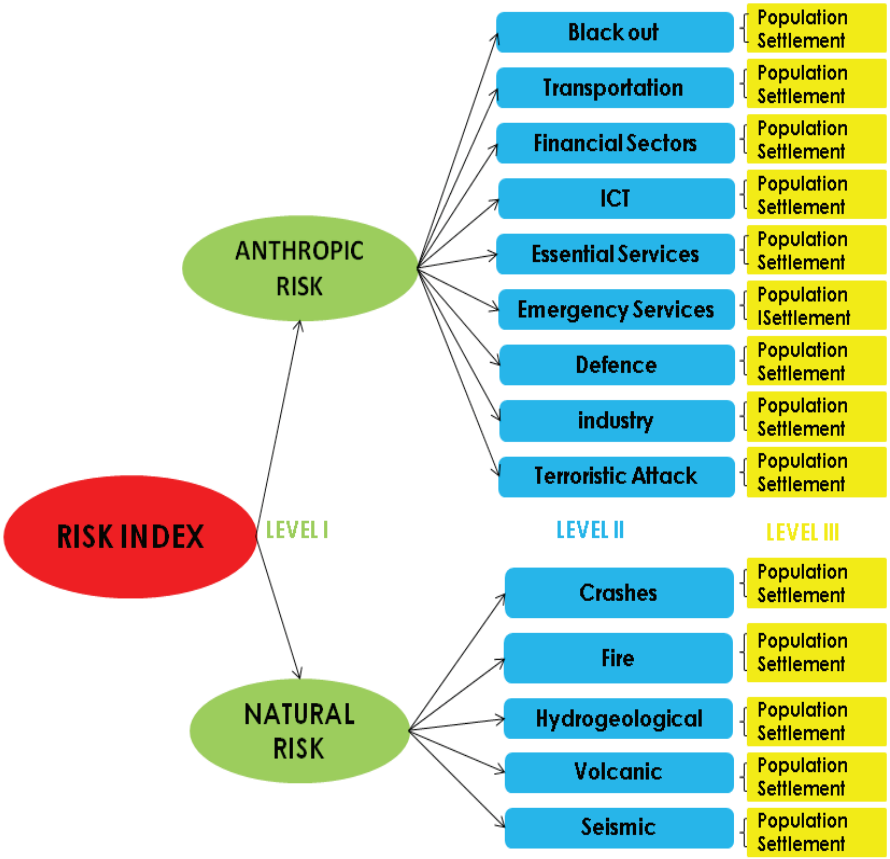

Figure 4: Levels I to III of the hierarchical tree.

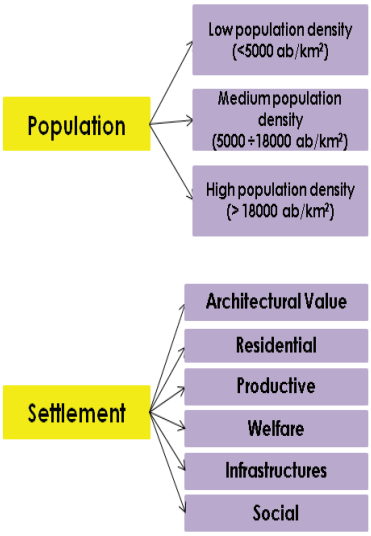

Figure 5: Level IV of the hierarchical tree.

Each level of the hierarchical tree has a pairwise comparison matrix. The matrices for each of the 32 quarters of Rome and the 22 districts of Centro Storico were compiled to compute the values of I_{Rn} and I_{Ra} (Figures 6 and 7). The results obtained clearly show that anthropic risk is comparable to natural risk. Indeed, in areas in which there are many buildings of public interest, anthropic risk is much higher than natural risk. As we can see from the graphs, I_{Rn} is very high in areas that are located near the Tiber and Aniene Rivers, while I_{Ra} is higher in zones where critical infrastructures are concentrated.

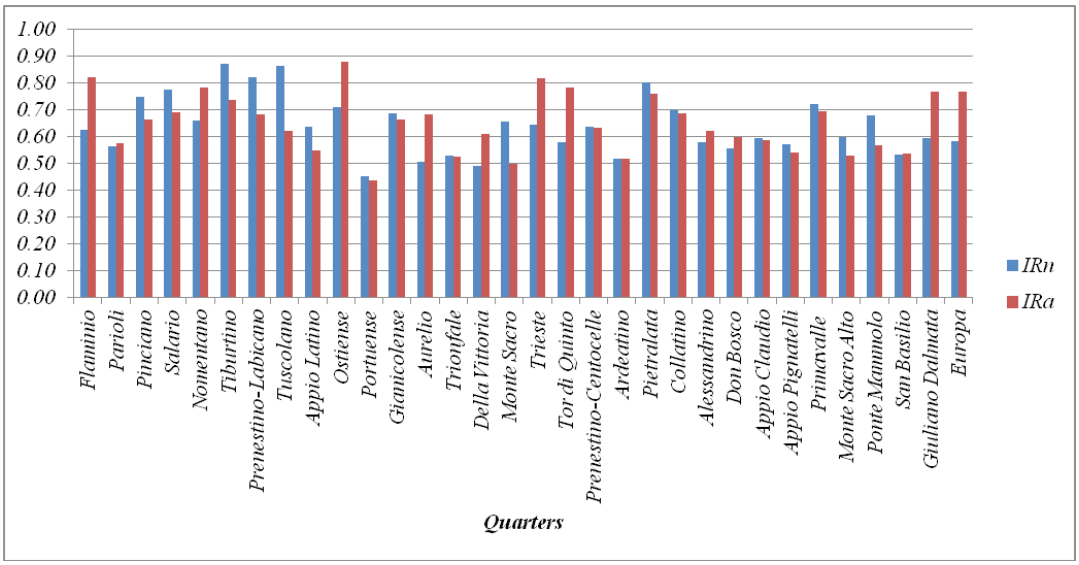

Figure 6: Risk indices of Rome's quarters.

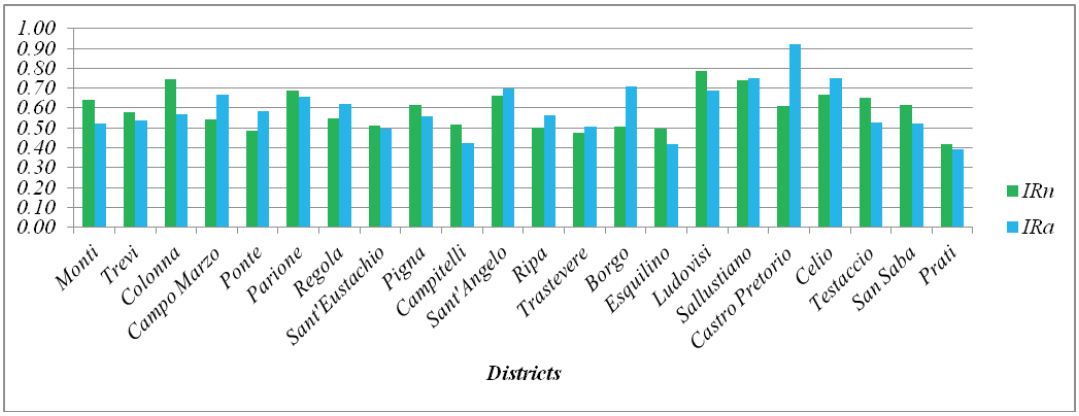

Figure 7: Risk indices of Centro Storico's districts.

5. CONCLUSION

In big metropolises, there are various state organs, public and private agencies, and critical infrastructures that are crucial to the stability of the respective cities, and sometimes of the state. Therefore, as the cities have much vulnerability, the territorial stability could be compromised if even one of its structural elements does not function. The critical infrastructures of Rome, as well as those of any large city, are linked by a closely-knit network of interconnections that are difficult to analyse. If we evaluate the vulnerability of an element outside of its context, we may underestimate the existent risks and be unable to assess the problems that could cause its collapse. AHP allowed us to analyse each risk element according to its importance in the system. We were able to estimate the systemic vulnerability, compare elements that are very different from each other, and finally, demonstrate that emergency planning is equally important for both natural and anthropic risks.

REFERENCES

Facolne, D., De Felice, F. & Saaty, T.L. (2009). *Il Decision Making e i Sistemi Decisionali Multicroterio.* Ulrico Hoepli, Milano.

Fanizzi, L. & Misceo, S. (2010). L'applicazione dell'Analytic Hierarchy Process (AHP) nella valutazione ambientale iniziale. *Scienza & Inquinamento*, **4**: 1:7.

Mugavero R. & Sabato V., (2011). *Planning and Risk Management of Urban Crisis for Rome City: Applications of the AHP Model and Design of the Control Room*. PhD Thesis, Department of Electronic Engineering, University of Rome "Tor Vergata", Italy.

Ragheb, M. (2011). *Probabilistic, Possibilistic and Deterministic Safety Analysis: Nuclear Applications*. Department of Nuclear, Plasma and Radiological Engineering, University of Illinois at Urbana-Champaign, Urbana, Illinois.

Roma Capitale (2012). *Roma Capitale*. Available online at: http://www.comune.roma.it (Last access date: 12 March 2012).

Saaty, T.L. (1996). *Theory and Applications of the Analytic Network Process: Decision Making with Benefits, Opportunities, Costs, and Risks.* RWS Publications, Pittsburgh.

Torre, C., Orlando, G., Selicato, F. & Reina, A., (2005). Valutazione del rischio e pianificazione territoriale: approcci multi criteriali e gis-based per la valutazione del danno potenziale. *Incontro di Studio del Ce.S.E.T.*, **35:** 173-192.

United Nations Disaster Relief Office (UNDRO) (1979). *Natural Disasters and Vulnerability Analysis*. United Nations Disaster Relief Office (UNDRO), Geneva.

STATISTICAL ANALYSIS OF ELEVATION VARIANCES OF CELLS OF PHYSIOGRAPHIC FEATURES EXTRACTED FROM MULTISCALE DIGITAL ELEVATION MODELS

Dinesh Sathyamoorthy

Instrumentation & Electronics Technology Division (BTIE), Science & Technology Research Institute for Defence (STRIDE), Ministry of Defence, Malaysia

*E-mail: dinesh.sathyamoorthy@stride.gov.my

ABSTRACT

While a number of studies have been conducted on classification on various landforms extracted from multiscale digital elevation models (DEMs), not much attention has been provided on the effect of multiscaling on elevation variances. To this end, in this paper, the statistical analysis of elevation variances of cells of physiographic features extracted from multiscale DEMs is conducted. Six statistical parameters are analysed, namely mean, standard deviation, skewness, kurtosis, energy and entropy. For the respective multiscale DEMs and predominant physiographic features (mountains, basins and piedmont slopes), varying patterns are observed with increasing scale due to varying surface profiles and the changes that occur over the scales. For all the parameters, with the exception of mean elevation, the DEMs and mountains exhibit similar patterns at the initial scales, indicating that mountains are the more dominant of the three predominant physiographic features in deciphering terrain character. The loss of fine detail during multiscaling causes the mean elevations of the DEMs and mountains to decrease. Elevation gain due to removal of concave regions causes the mean elevation of the basins to increase. The mean elevation of the piedmont slopes initially increases due to the removal of concave regions, but then decreases drastically due to the removal of fine detail. Energy and entropy prove to be effective surface roughness measures, providing decreasing roughness values for the DEMs and physiographic features over the scales. On the other hand, standard deviation of elevation is found to be an ineffective surface roughness measure as it fails to quantitatively discriminate between surfaces of different amplitudes, frequencies and correlations, and is sensitive to abrupt strong variations in elevation. Values of skewness and kurtosis over the scales indicate that elevation distributions decrease at higher rates as compared to mean elevations for the DEMs and mountains, lower for the piedmont slopes, and similar for the basins.

Keywords: *multiscale digital elevation models (DEMs); physiographic features; elevation variances; cells; surface roughness.*

1. INTRODUCTION

Scale variations can constrain the detail with which information can be observed, represented and analysed. The term scale refers to a combination of both spatial extent, and spatial detail or resolution (Goodchild & Quattrochi, 1997; Tate & Wood, 2001; Li *et al*., 2005; Drăguţ & Eisank, 2011). Changing the scale without first understanding the effects of such an action can result in the representation of patterns or processes that are different from those intended due to loss of detail, and variations in terrain parameters and landforms (Robinson *et al*., 1984; Lam & Quattrochi, 1992; Goodchild & Quattrochi, 1997; Lam *et al*., 2004; Summerfield, 2005; Wu *et al*., 2008; Drăguţ *et al*., 2009; Dragut & Eisank, 2011). Hence, feature detection and characterisation often need to be performed at different of scales measurement. Wood (1996a, b), Wu *et al*. (2008), Drăguţ *et al*. (2009) and Drăguţ & Eisank (2011) demonstrated that analysis of a location at multiple scales allows for a greater amount of information to be extracted from a digital elevation model (DEM) about the spatial characteristics of a feature.

While a number of studies have been conducted on classification of various landforms extracted from multiscale DEMs (Sagar *et al.*, 2003; Fisher *et al.*, 2004, 2005; Tay *et al.*, 2005; Schmidt & Andrew, 2005; Dinesh, 2007, 2010; Behrens *et al.*, 2010; Dinesh *et al.*, 2011), not much attention has been provided on the effect of multiscaling on elevation variances. To this end, in this paper, the statistical analysis of elevation variances of cells of physiographic features extracted from multiscale DEMs is conducted. Physiography (also known as land surface characteristics) is the study of the physical features and attributes of the earth's land surface. The detection of the physiographic features of a terrain is the first phase involved in the classification of the various landforms of the terrain. A terrain can be segmented into three predominant physiographic features; mountains, piedmont slopes and basins (Miliaresis & Argialas, 1999; Dinesh *et al.*, 2007).

2. STATISTICAL PARAMETERS ANALYSED

The most common method to extract statistical parameters of an image is by employing the first order distribution $P(b)$ of the intensities of the image. DEMs are greyscale images with the intensity of each cell representing elevation at the corresponding location. For each elevation b in the elevation range (b_{min} to b_{max}) of a region with area of M cells, $P(b)$ is computed as follows:

$$P(b) = \frac{N(b)}{M} \tag{1}$$

where $N(b)$ is the number of cells with elevation b.

The computed values of $P(b)$ are used to compute the following parameters (Pratt, 2001; Aria *et al.*, 2004; Smith *et al.*, 2009):

2.1 Measures of Centrality and Variability

Mean S_M (Equation 2) provides the numerical average of the set of elevation values of the DEM, and indicates where the distribution of the elevations is centred. Standard deviation S_D (Equation 3) indicates the variability of the distribution from the mean. It is often used as a measure of surface roughness, quantifying the vertical deviations of the surface from its best-fit plane, represented by the mean (Bennett, 1992; Yokota *et al.,* 2008; Grohmann *et al.*, 2011).

$$S_M = \bar{b} = \sum_{b=b_{\min}}^{b_{\max}} b \bullet P(b) \tag{2}$$

$$S_D = \sigma_b = \sqrt{\sum_{b=b_{\min}}^{b_{\max}} (b - \bar{b})^2 \bullet P(b)} \tag{3}$$

2.2 Measures of Distribution Shape

Skewness S_S (Equation 4) characterises the degree of asymmetry of the elevation distribution around the mean. A distribution that is symmetric about the mean has skewness of 0. Values greater than 0 indicate skewness of distributions to the right of the mean, while values less than 0 indicate skewness to the left.

$$S_S = \frac{1}{\sigma_b^{\,3}} \bullet \sum_{b=b_{\min}}^{b_{\max}} (b - \bar{b})^3 \bullet P(b) \tag{4}$$

Kurtosis S_K (Equation 5) is a measure the relative peakedness of a distribution relative to the normal distribution. The kurtosis of a normal distribution is 0. Distributions that are more outlier-prone than the normal distribution have kurtosis greater than 0, while lower outlier-prone distributions have kurtosis less than 0.

$$S_K = \langle \frac{1}{\sigma_b^{\,4}} \bullet \sum_{b=b_{\min}}^{b_{\max}} (b - \bar{b})^4 \bullet P(b) \rangle - 3 \tag{5}$$

2.3 Measures of Complexity

Energy S_N (Equation 6) provides a measure of repeated transitions in the distributions. Energy is a measure of surface roughness, with a higher value indicating a higher rate of repeated transitions and hence, decreased surface roughness, and vice versa.

$$S_N = \sum_{b=b_{\min}}^{b_{\max}} P(b)^2 \tag{6}$$

Entropy S_E (Equation 7) is a measure of randomness that can be used to characterise the elevation variation of a DEM. It provides a low value when the elevations have similar values, and a high value when the elevations vary significantly. Entropy is also often used as a measure of surface roughness (Papasaika & Baltsavias, 2009; Gorini, 2009; Ahmad Fadzil *et al.*, 2011).

$$S_E = \sum_{b=b_{\min}}^{b_{\max}} P(b) \bullet \log_2[P(b] \tag{7}$$

3. METHODOLOGY

3.1 Data Set

The DEM in Figure 1 shows the area of Great Basin, Nevada, USA. The area is bounded by latitude 38° 15' to 42° N and longitude 118° 30' to 115° 30'W. The DEM was rectified and resampled to 925 m in both *x* and *y* directions. The DEM is a Global Digital Elevation Model (GTOPO30) and was downloaded from the USGS GTOPO30 website (GTOPO30, 1996). GTOPO30 DEMs are available at a global scale, providing a digital representation of the Earth's surface at a 30 arc-seconds sampling interval. The land data used to derive GTOPO30 DEMs are obtained from digital terrain elevation data (DTED), 1-degree DEMs for USA and the digital chart of the world (DCW). The accuracy of GTOPO30 DEMs varies by location according to the source data. The DTED and the 1-degree dataset have a vertical accuracy of ±30 m while the absolute accuracy of the DCW vector dataset is ±2,000 m horizontal error and ±650 m vertical error (Miliaresis & Argialas, 2002). Tensional forces on the terrain's crust and thins by normal faulting cause the formation an array of tipped mountain blocks that are separated from broad plain basins, producing a basin-and-range physiography (Howell, 1995; Summerfield, 1996, 2000; Miliaresis & Argialas, 1999; Miliaresis, 2008).

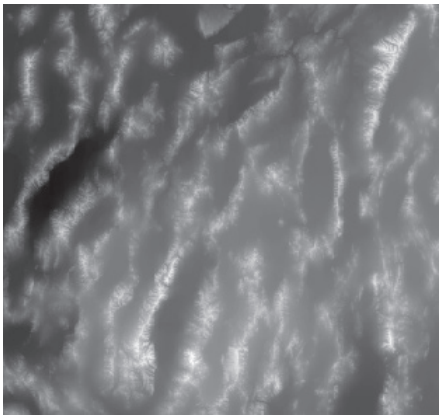

Figure 1: The GTOPO30 DEM of Great Basin. The elevation values of the terrain (minimum 1,005 m and maximum 3,651 m) are rescaled to the interval of 0 to 255 (the brightest pixel has the highest elevation). The scale is approximately 1:3,900,000.

3.2 Generation of Multiscale DEMs

In this paper, multiscaling is performed using the lifting scheme (Sweldens, 1996, 1997). The lifting scheme is a flexible technique that has been used in several different settings, for easy construction and implementation of traditional wavelets and of second-generation wavelets, such as spherical wavelets. It has proven to be a powerful multiscale analysis tool in image and signal processing (Claypoole & Baraniuk 2000, Starck 2002, Guo *et al*. 2008), which has received recent attention in geospatial analysis (Dinesh, 2007, 2010; Hayat *et al*., 2008; Bernadin *et al*., 2008; Yang *et al*., 2009; Dinesh *et al.*, 2011; Ahmad Fadzil *et al*., 2011). This is due to ability to preserve accurate surface profiles, in terms of waveform, shape and amplitude, without causing boundary destruction (Jiang *et al.*, 2001a,b; Nonomura *et al.*, 2010). Lifting consists of the following three basic operations:

i. Step 1: Split

The original data set $x[n]$ is divided into two disjoint subsets, even indexed points $x_e[n]=x[2n]$, and odd indexed points $x_0[n]=x[2n+1]$.

ii. Step 2: Predict

The odd and even subsets are often highly correlated. This correlation structure typically local and hence, it is possible to accurately predict the wavelet coefficients $d[n]$ as the error in predicting $x_0[n]$ from $x_e[n]$ using the prediction operator $P(x_e[n]$. The predict step uses a function that approximates the data set (Equation 8). The difference between the approximation and the actual data replaces the odd elements of the data set (Equation 9). The even elements are left unchanged and become the input for the next step in the transform.

$$P(x_e[n]) = \frac{1}{2}(x_e[n] + x_e[n+1]) \quad (8)$$

$$d[n] = x_0[n] - P(x_e[n])$$
$$d[n] = x_o[n] - P(x_e[n])d[n] = x_o[n] - P(x_e[n]) \quad (9)$$

iii. Step 3: Update

The update step replaces the even elements with an average. This results in a smoother output $c[n]$ that represents a coarse approximation to the signal $x[n]$. The update operator U is applied to the wavelet coefficients (Equation 10), and is added to $x_e[n]$ (Equation 11).

$$U(d[n]) = \frac{1}{4}(d[n-1] + d[n+1]) \quad (10)$$

$$c[n] = x_e[n] + U(d[n]) \quad (11)$$

The above three steps form a lifting stage. A simple worked example of the algorithm is provided in the appendix. The lifting scheme scans 2D images row-by-row. Using a DEM as the input, an iteration of the lifting stage generates the complete set of multiscale DEMs $c_s[n]$ and the elevation loss caused by the change of scale $d_s[n]$. At each iteration, $c_s[n]$ only contains half of the points of the input for the iteration, and hence, the resolution of the generated multiscale DEM is reduced by half.

Multiscale DEMs of the Great Basin region are generated by implementing the lifting scheme for scales r of 1 to 20. As shown in Figure 2, as the scale increases, the merging of small regions into the surrounding grey level regions increases, causing removal of fine detail in the DEM. As a result, the generated multiscale DEMs possess lower resolutions at higher degrees of scaling.

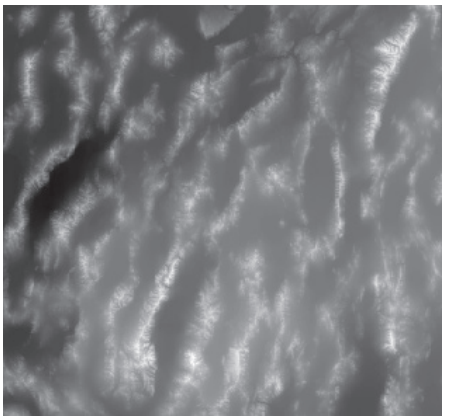

(a)

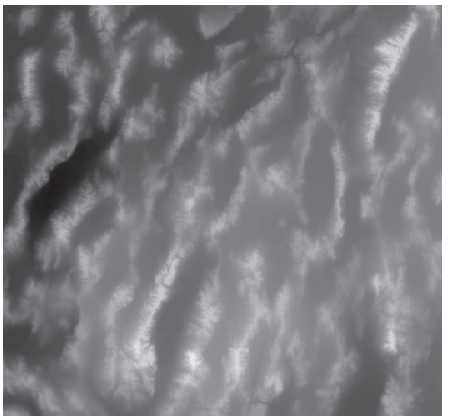

(b)

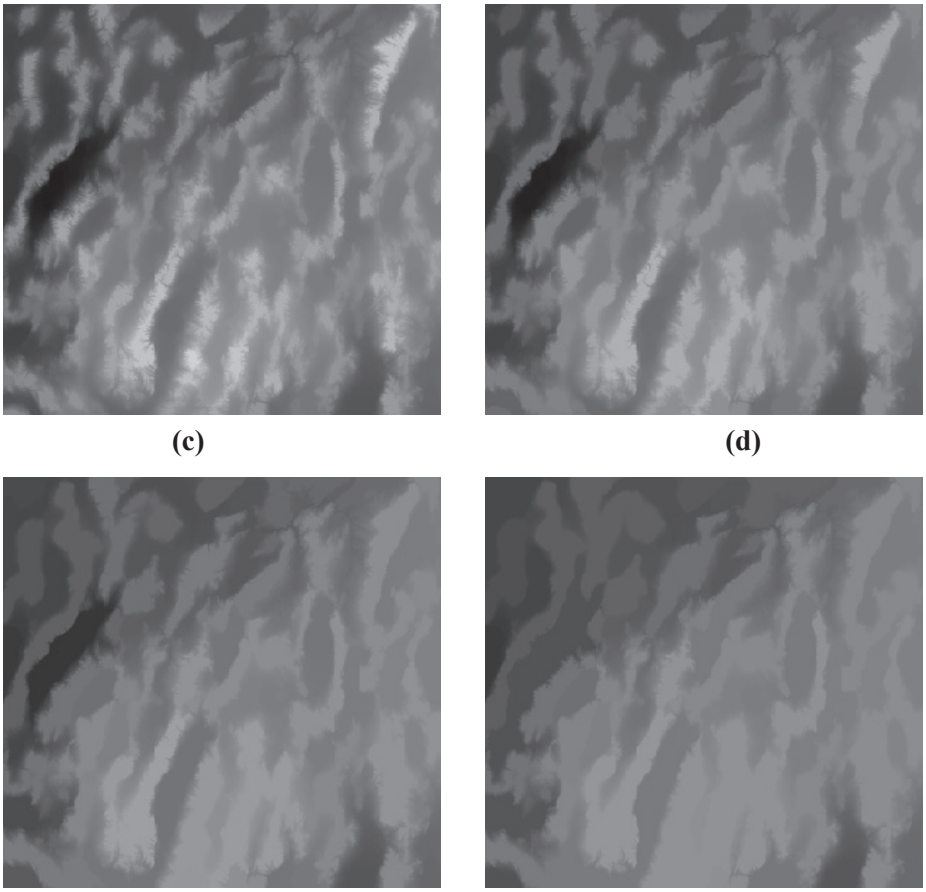

(c) **(d)**

(e) **(f)**

Figure 2: Multiscale DEMs generated using scales of (a) 1; (b) 3; (c) 5; (d) 10; (e) 15; and (f) 20.

3.2 Extraction of Physiographic Features

The mountains, basins and piedmont slopes of the generated multiscale DEMs are extracted using the mathematical morphological based physiographic segmentation algorithm proposed in Dinesh *et al*. (2007). Ultimate erosion is used to extract the peaks and pits of the DEM. Conditional dilation is performed on the peaks and pits of the DEM to obtain the mountain and basin cells respectively. The cells that are not classified as mountain cells or basin cells are assigned as piedmont slope cells.

As shown in Figure 3, the merging of small regions into the surrounding grey level regions and hence, removal of fine detail in the DEM, causes a reduction in the area of the extracted mountains, and an increase in the area of the extracted basins. In general, the area of the piedmont slopes remains fairly constant, but the pattern of the piedmont slopes changes significantly based on the change in pattern of the mountains and basins.

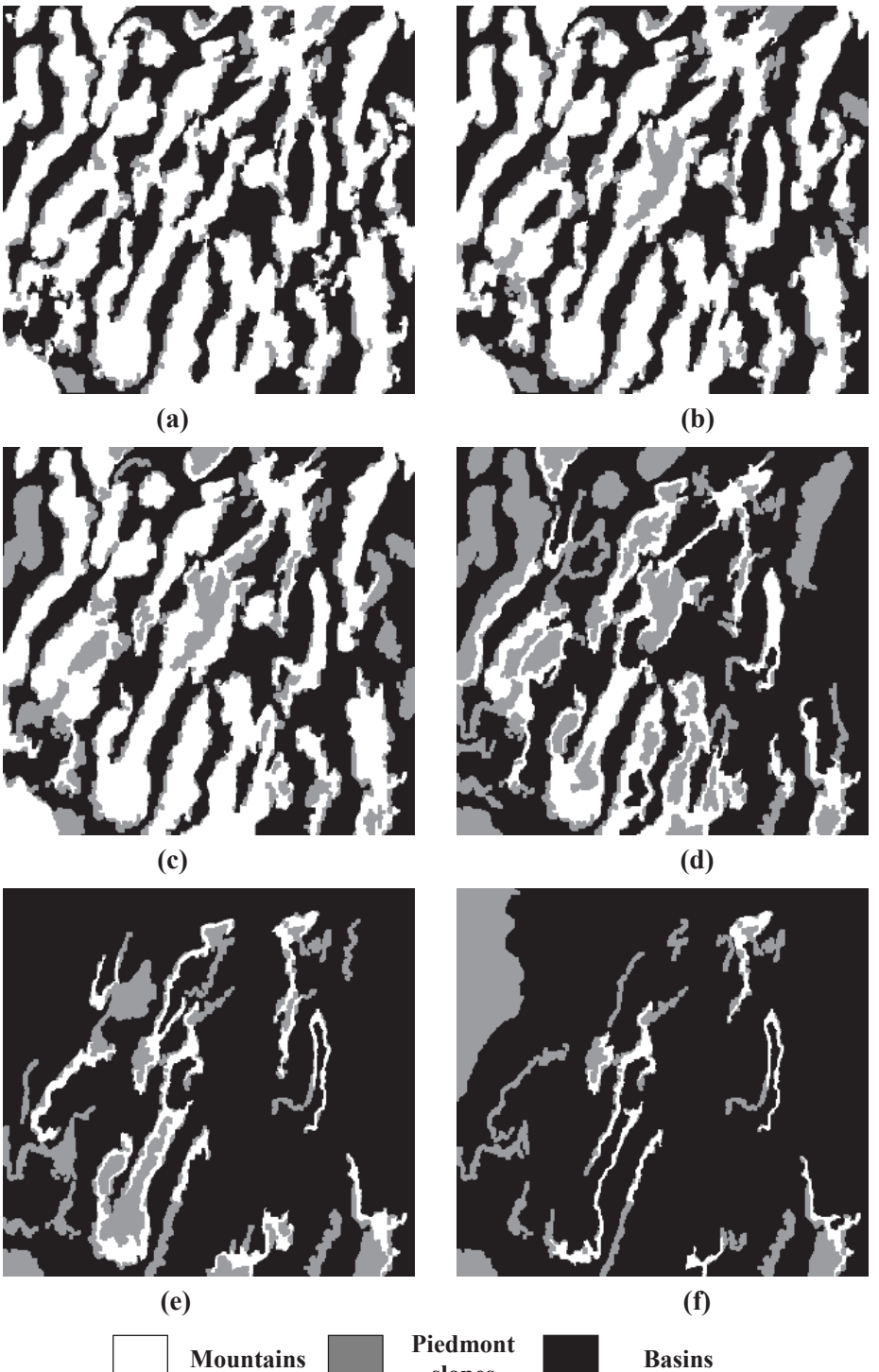

Figure 3: Physiographically segmented terrains of the corresponding multiscale DEMs in Figure 2.

4. RESULTS AND DISCUSSION

The computed statistical parameters of the generated multiscale DEMs and the corresponding extracted physiographic features are shown in Figure 4. For the respective DEMs and physiographic features, varying patterns are observed in the plots due to varying surface profiles, and the changes that occur over the scales. For all the parameters, with the exception of mean elevation, the DEMs and mountains exhibit similar patterns at the initial scales, indicating that mountains are the more dominant of the three predominant physiographic features in deciphering terrain character.

As expected, mountains have the highest mean elevations as compared to the other features over the scales (Figure 4(a)). The mean elevations for the DEMs and mountains decrease with increasing scale due to the removal of fine detail. However, for basins, the mean elevations increase over scale, as the removal of fine detail causes the removal of concave regions, resulting in increased elevations in the basin regions. The mean elevations of the piedmont slopes increase at the initial scales due to the removal of concave regions, but then decrease drastically due to the removal of fine detail in these regions.

Standard deviation, energy and entropy are measures of surface roughness. It is expected that increase in scale will result in decreased surface roughness for the DEMs and physiographic features due to the removal of curvature regions, and hence, reduced vertical deviations from the best-fit plane.

The entropy of the DEMs and physiographic features show the expected results, providing decreasing values over scale (Figure 4(f)). The DEMs and mountains have higher entropy values compared to the basins and piedmont slopes until the final three scales, where the mountains regions have largely been removed.

The energies of the DEMs and physiographic features (Figure 4(e)) increase over the scales, indicating increased occurrences of repeated elevation transitions between the cells and hence, reduced surface roughness. The DEMs and mountains exhibit lower energies, and hence, higher surface roughness, as compared to the basins and piedmont slopes.

The standard deviations (Figure 4(b)) of the DEMs and mountains decrease with increasing scale. While both show similar values at the initial scales, the standard deviations of the mountains then decrease drastically, having significantly lower values than the basins and piedmont slopes. Despite the removal of curvature regions, the basins and piedmont slopes have increasing standard deviations at the initial scales, after which the basins have reducing values and the piedmont slopes have fluctuating values. The accuracy of standard deviation of elevation as a measure of surface roughness has been called into question as it fails to quantitatively

discriminate between surfaces of different amplitudes, frequencies and correlations, and is sensitive to abrupt strong variations in elevation (Hoffman & Krotkov, 1990; Shepard *et al.*, 2001; Ahmad Fadzil *et al.*, 2011; Grohmann *et al.*, 2011).

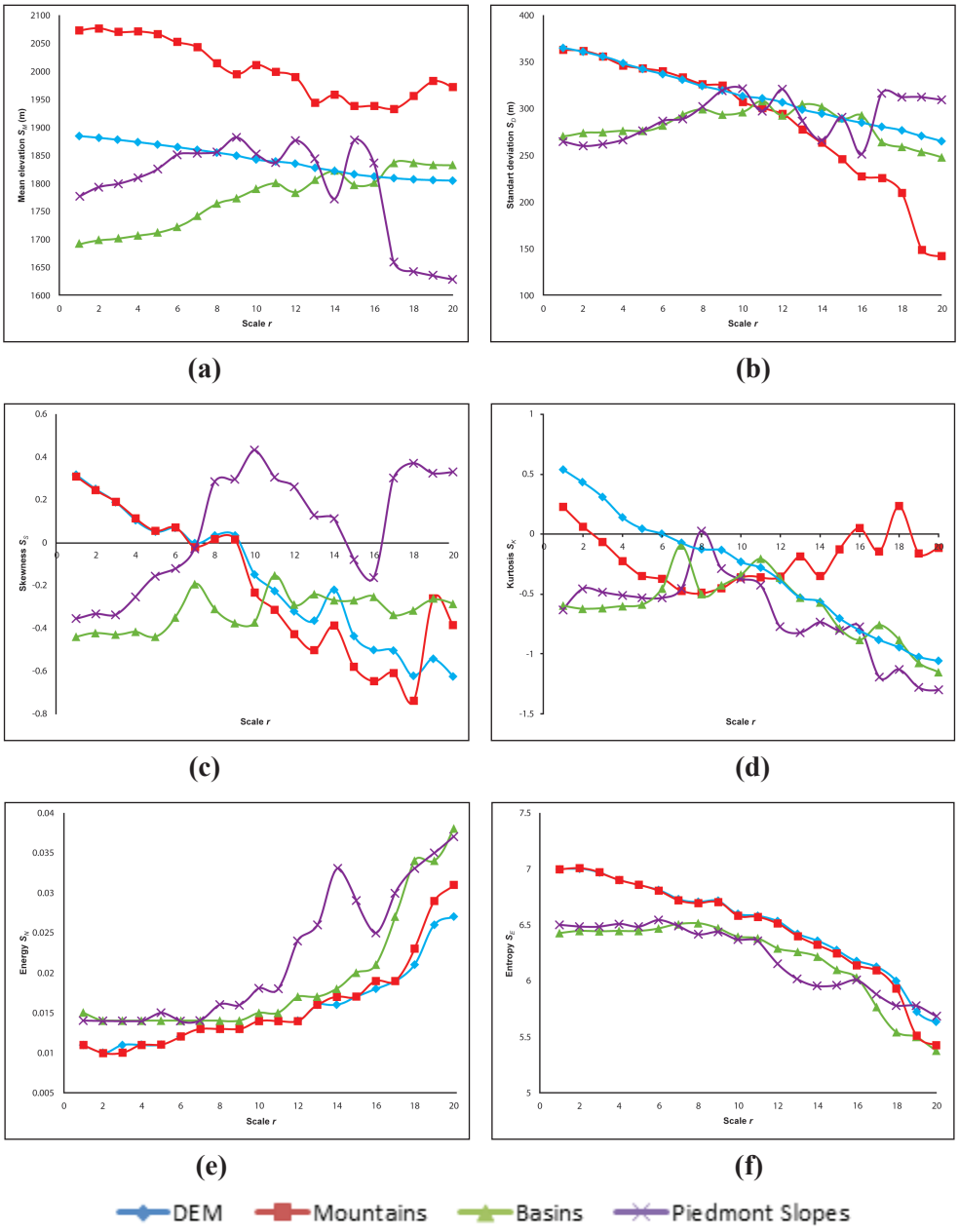

Figure 4: Computed statistical parameters of the generated multiscale DEMs and the corresponding extracted physiographic features: (a) Mean; (b) Standard Deviation; (c) Skewness; (d) Kurtosis; (e) Energy; (f) Entropy.

Changes in values of skewness and kurtosis over the scales are dependent on the rate of changes of elevation distributions and mean elevations. As shown in Figure 4(c), the DEMs and mountains initially have positive skewness values, which then decrease with increasing scales to negative values, indicating that the elevation distributions decrease at higher rates as compared to the mean elevations. The skewness values of the piedmont slopes increase from being initially negative to positive, indicating that the elevation distributions decrease at a lower rate as compared to the mean elevations. The skewness values for the basins remains relatively constant with some fluctuations, indicating that the elevation distributions and mean elevations increase at similar rates.

For kurtosis (Figure 4(d)), at the initial scale, the DEMs and mountains have initial values that are larger than 0 due to the elevation distributions being higher than the mean elevations, while the basins and piedmont slopes have initial value that are smaller than 0 due to the elevation distributions being lower than the mean elevations. The kurtosis values for the DEMs and mountains decrease at the initial scales due to the elevation distributions reducing at higher rates as compared to the mean elevations. The kurtosis values of the DEMs then continue to decrease, but increase for the mountains due to the reduction in area of mountains. The kurtosis values for the basins and piedmont slopes increase at the initial scales as the elevation distributions become closer the means elevations. The kurtosis values for the piedmont slopes then decreases as the elevations in these regions decrease, while the values for the basins also decrease due to the increase in area of basins.

4. CONCLUSION

This study has provided key insights into the statistical behaviour of elevation variances of cells of physiographic features extracted from multiscale DEMs. The loss of fine detail during multiscaling causes the mean elevations of the DEMs and mountains to decrease. Elevation gain due to removal of concave regions causes the mean elevation of the basins to increase. The mean elevation of the piedmont slopes initially increases due to the removal of concave regions, but then decreases drastically due to the removal of fine detail. Energy and entropy proved to be effective surface roughness measures, providing decreasing roughness values for the DEMs ad physiographic features over the scales. On the other hand, standard deviation of elevation was found to be an ineffective surface roughness measure as it fails to quantitatively discriminate between surfaces of different amplitudes, frequencies and correlations, and is sensitive to abrupt strong variations in elevation. Values of skewness and kurtosis over the scales indicate that elevation distributions decrease at higher rates as compared to mean elevations for the DEMs and mountains, lower for the piedmont slopes, and similar for the basins.

For the purposes of this study, the analysis was conducted for a mountainous terrain, with rough surface profile. For future work, the analysis will be extended to terrains of varying profiles and character.

ACKNOWLEDGEMENT

The author is grateful to the reviewers, Dr. Mahdi Che Isa and Mdm. Nor Hafizah Mohamed, for their suggestions that have helped strengthen this manuscript.

REFERENCES

Ahmad Fadzil, M.H., Dinesh, S. & Vijanth Sagayan, A. (2011). A method for computation of surface roughness of digital elevation model terrains via multiscale analysis. *Comput. Geosci.*, **37**: 177-192.

Aria, E.H., Saradjian, M.R., Amini, J. & Lucas, C. (2001). Generalized cooccurrence matrix to classify IRS-1D images using neural network. *XXth ISPRS Congress*, 12-23 July 2004 Istanbul, Turkey.

Bennett, J.M. (1992). Recent developments in surface roughness characterization. *Meas. Sci. Technol.*, **3**: 1119-1127.

Behrens, T., Zhu, A.X., Schmidt, K. & Scholten, T. (2010). Multi-scale digital terrain analysis and feature selection for digital soil mapping. *Geoderma*, **155**: 175-185.

Bernardin, T., Cowgill, E. S., Gold, R. D., Hamann, B., Kreylos, O. & Schmitt, A., 2008. Real-time terrain mapping. *In*: H. Hagen, ed., *Scientific Visualization: Challenges for the Future*. IEEE Computer Society Press, Los Alamitos, California, pp. 275-288.

Claypoole, R.L. & Baraniuk, R.G. (2000). A multiresolution wedgelet transform for image processing. *In* Unser, M.A., Aldroubi, A. & Laine, A.F. (Eds.), *Wavelet Applications in Signal and Image Processing VIII, Volume 4119 of SPIE Proceedings*. SPIE, Bellingham, Washington, pp. 253-262.

Dinesh, S. (2007). Characterization of catchments extracted from multiscale digital elevation models. *Appl. Math. Sci.*, **1**: 963-974.

Dinesh, S. (2010). Morphological spatial analysis of mountains extracted from multiscale digital elevation models. *J. Defence Secur.*, **1**: 220-237

Dinesh, S., Radhakrishnan, P. & Sagar, D.S.D. (2007). Morphological segmentation of physiographic features from DEM. *Int. J. Remote Sens.*, **28**: 3379-3394.

Dinesh, S., Ahmad Fadzil, M.H. & Vijanth Sagayan, A. (2011). Computation of uncertainty of physiographic features extracted from multiscale digital

elevation models using fuzzy classification. *Image Processing, Image Analysis and Real-Time Imaging (IPIARTI) Symposium 2011*, 6 October 2011, Multimedia University (MMU), Cyberjaya.

Drăguţ, L. & Eisank, C. (2011). Object representations at multiple scales from digital elevation models. *Geomorphology*, **129**: 183-189.

Drăguţ, L., Tiede, D. & Levick, R. (2009). ESP: A tool to estimate scale parameter for multiresolution image segmentation of remotely sensed data. *Int. J. Geogr. Inf. Sci.*, **24**: 859-871.

Fisher, P., Wood, J. & Cheng, T. (2004). Where is Helvellyn? Multiscale morphometry and the mountains of the English Lake District. *T. I. Brit. Geogr.*, **29**: 106-128.

Fisher, P., Wood, J. & Cheng, T., 2005. Fuzziness and ambiguity in multi-scale analysis of landscape morphometry. *In*: Cobb, M and Petry, F and Robinson, V, (eds.), *Fuzzy Modeling with Spatial Information for Geographic Problems*. Springer, New York, pp. 209 - 232.

Goodchild, M.F. & Quattrochi, D.A. (1997). Scale, multiscaling, remote sensing and GIS. *In* Quattrochi, D.A. and Goodchild, M.F. (Eds.), *Scale in Remote Sensing and GIS*. Lewis Publishers, Boca Raton, Florida, pp. 1-11.

Gorini, M.A.V. (2009). Physiographic classification of the ocean floor: A multi-scale geomorphometric approach. *Geomorphometry 2009*, 31 August – 2 September 2009, Zurich, Switzerland.

Grohmann, C.H., Smith, M.J. & Riccomini, C. (2011). Multiscale analysis of topographic surface roughness in the Midland Valley, Scotland. *IEEE T. Geosci. Remote Sens.*, **49**: 1200-1213.

GTOPO30 (1996). *GTOPO30: Global 30 Arc Second Elevation Data Set*. Available online at: http://edcwww.cr.usgs.gov/landdaac/gtopo30/gtopo30.html (Last access date: 1 June 2009).

Guo, S.M., Chang, W.H., Tsai, J.S.H., Zhuang, B.L. & Chen, L.C., 2008. JPEG 2000 wavelet next term filter design framework with chaos evolutionary programming. *Signal Process.*, **88**: 2542-2553.

Hayat, K, Puech, W. & Gesquère, G., 2008. Scalable 3-D terrain visualization through reversible JPEG2000-based blind data hiding. *IEEE T. Multimedia*, **10**: 1261-1276.

Hoffman, R. & Krotkov, E. (1990). Terrain roughness measurement from elevationMaps. *In* Chun, W. H. & Wolfe, W.J. (Eds.), *Proceedings of the SPIE, Mobile Robots IV 1989, vol. 1195*, pp. 104–114.

Howell, D. (1995). *Principles of Terrain Analysis: New Applications for Global Tectonics*. Chapman and Hall, London.

Jiang, X.Q., Blunt, L. & Stout, K.J. (2001a). Application of the lifting scheme to rough surfaces. *Precis. Eng.*, **25**: 83-89.

Jiang, X.Q., Blunt, L. & Stout, K.J. (2001b). Lifting wavelet for three-dimensional surface analysis. *Int. J. Mach. Tool. Manu.*, **41**: 2163-2169.

Lam, N. & Quattrochi, D. (1992). On the issues of scale, resolution, and fractal analysis in the mapping science. *Prof. Geogr.*, **44**: 88-98.

Lam, N., Catts, D., Quattrochi, D, Brown, D. & McMaster, R. (2004). Scale. *In*: Rechcígl, M., McMaster, R.B., Usery, E.L. (Eds.), *A Research Agenda for Geographic Information Science*. CRC Press, New York, pp. 93-128.

Li, Z., Zhu, Q., & Gold, C. (2005). *Digital Terrain Modelling: Principles and Methodology*. CRC Press, New York.

Miliaresis G. (2008). Quantification of terrain processes. *Lect. Notes Geoinform. Cartogr.* **XIV**: 13-28.

Miliaresis, G. & Argialas, D.P. (1999). Segmentation of physiographic features from Global Digital Elevation Model/GTOPO30. *Comput. Geosci.*, **25**: 715-728.

Miliaresis, G. & Argialas, D.P. (2002). Quantitative representation of mountain objects extracted from the Global Digital Elevation Model (GTOPO30). *Int. J. Remote Sens.*, **23**: 949-964.

Nonomura, K., Ono, M., Zhou, L.B., Shimizu, J. & Ojima, H. (2010). Design of digital filters for Si wafer surface profile measurement - noise reduction by lifting scheme wavelet transform. *Adv. Mater. Res.*, **126-128**: 732-737.

Papasaika, H. & Baltsavias, E. (2009). Investigations on the relation of geomorphological parameters to DEM accuracy. *Geomorphometry 2009*, 31 August – 2 September 2009, Zurich, Switzerland.

Pratt, W.K. (2001). *Digital Image Processing*. John Wiley & Sons, New York.

Robinson, A.H., Sale, R.D., Morrison, J.L. & Muehrcke, P.C. (1984). *Elements of Cartography*. John Wiley & Sons, New York.

Sagar, B.S.D., Murthy, M.B.R., Rao, C. & Raj, B. (2003). Morphological approach to extract ridge-valley connectivity networks from digital elevation models. *Int. J. Remote Sens.*, **24**: 573-581.

Schmidt, J. & Andrew, R. (2005). Multi-scale landform characterization. *Area*, **37**: 341-350.

Shepard, M.K., Campbell, B.A., Bulmer, M.H., Farr, T.G., Gaddis, L.R. & Plaut, J.J. (2001). The roughness of natural terrain: A planetary and remote sensing perspective. *J. Geophys. Res.*, **106**: 32,777-32,795.

Smith, J.D.S., Goodchild, M.F. & Longley, P.A. (2009). *Geospatial Analysis: A Comprehensive Guide to Principles, Techniques and Software Tools*. Matador, Leicester.

Starck, J.L. (2002). Non linear multiscale transforms. *In* Barth, T.J., Chan, T. & Haimes, R. (Eds.), *Multiscale and Multiresolution Methods: Theory and Applications*. Springer, Heidelberg, Germany, pp. 239-266.

Summerfield, M. (1996). *Global Geomorphology*. Longman, Essex.

Summerfield, M. (Ed.) (2000). *Geomorphology and Global Tectonics*. John Wiley & Sons, New York.

Summerfield, M. (2005). A tale of two scales, or two geomorphologies. *T. I. Brit. Geogr.*, **30**: 402-415.

Sweldens, W. (1996). The lifting scheme: A custom-design construction of biothorgonal wavelets. *Appl. Comput. Harmonics Anal.*, **3**: 186-200.

Sweldens, W. (1997). The lifting scheme: A construction of second generation wavelets. *J.Math. Anal.*, **29**: 511-546.

Tate, N., & Wood, J. (2001). Fractals and scale dependencies in topography. *In*: Tate, N., Atkinson, P. (Eds.), *Modelling Scale in Geographical Information Science*, Wiley, Chicester, pp. 35-51.

Tay, L. T., Sagar, B.S.D. & Chuah, H.T. (2005). Analysis of geophysical networks derived from multiscale digital elevation models: A morphological approach. *IEEE Geosci. Remote Sens. Lett.*, **2**: 399-403.

Wood, J. (1996a). Scale-based characterization of digital elevation models. *In*: Parker, D. (Eds.), *Innovation in GIS 3*. Taylor & Francis, London, pp. 163-175.

Wood, J. (1996b). *The Geomorphological Characterisation of Digital Elevation Models*. PhD Dissertation, University of Leicester, Leicester.

Wu, S., Li, J. & Huang, G.H. (2008). A study on DEM-derived primary topographic attributes for hydrologic applications: Sensitivity to elevation data resolution. *Appl. Geogr.*, **28**: 210-223.

Yang, Z., Liu, H., Yang, N. & Xiao, X. (2009). Study on multiscale generalization of DEM based on lifting scheme. *In* Liu, Y. & Tang, X. (Eds.), *Proceedings of the SPIE, Volume 7492*. SPIE, Bellingham, Washington, pp. 74922E-74922E-6.

Yokota, Y., Haruyama, J., Honda, C., Morota T., Ohtake, M., Kawasaki, H., Hara, S., Hioki, K. & LISM Working Group (2008). Lunar topography: Statistical analysis of roughness next term on a kilometer scale. *Adv. Space Res.*, **42**: 259-266.